

Nonlinear parametric modeling of suspension bridges under aeroelastic forces: torsional divergence and flutter

Andrea Arena · Walter Lacarbonara

Received: 18 March 2012 / Accepted: 1 October 2012 / Published online: 24 October 2012
© Springer Science+Business Media Dordrecht 2012

Abstract A fully nonlinear model of suspension bridges parameterized by one single space coordinate is proposed to describe overall three-dimensional motions. The nonlinear equations of motion are obtained via a direct total Lagrangian formulation and the kinematics, for the deck-girder and the suspension cables, feature the finite displacements of the associated base lines and the flexural and torsional rotations of the deck cross-sections assumed rigid in their own planes. The strain-displacement relationships for the generalized strain parameters, the elongations in the cables, the deck elongation, and the three curvatures, retain the full geometric nonlinearities. The proposed nonlinear model with its full extensional-flexural-torsional coupling is employed to study the torsional divergence caused by the static part of the wind-induced forces. Two suspension bridges are considered as case studies: the Runyang bridge (main span 1,490 m) and the Hu Men bridge (main span 888 m) in China. The evaluation of the onset of the static instability and the post-critical behavior takes into account the prestressed condition of the bridge subject to dead loads. The dynamic bifurcation that occurs at the onset of

flutter is also studied accounting for the prestressed equilibrium state about which the equations of motion are obtained via an updated Lagrangian formulation. Such a bifurcation is investigated in the context of the parametric nonlinear model considering the model parameters of the Runyang Suspension Bridge together with its aeroelastic derivatives. The calculated critical wind speeds for the onset of the static and dynamic bifurcations are compared with the results obtained via linear analysis and the main differences are highlighted. Parametric sensitivity studies are carried out to assess the influence of the design parameters on the instabilities associated with the bridge aeroelastic response.

Keywords Suspension bridges · Special Cosserat theory of beams · Nonlinear suspension cables · Geometrically exact approach · Aeroelastic derivatives · Torsional divergence · Flutter

1 Introduction

Structures possessing high bending torsional flexibility, such as suspension bridges, when subjected to wind-induced excitations can be affected by elastic instability phenomena such as torsional divergence or flexural-torsional flutter. In long- and super long-span suspension bridges, the geometric nonlinearities induced by the suspension cables and the high flexural-torsional slenderness of the deck play an important

A. Arena · W. Lacarbonara (✉)
Dipartimento di Ingegneria Strutturale e Geotecnica,
University of Rome La Sapienza, via Eudossiana, 18,
Rome 00184, Italy
e-mail: walter.lacarbonara@uniroma1.it

A. Arena
e-mail: andrea.arena@uniroma1.it

role in the static and dynamic response of the bridge. Moreover, the nonlinear effective stiffness of the structure in its prestressed equilibrium configuration under dead loads can strongly influence the behavior under both autonomous forces (e.g., aeroelastic loads) and nonautonomous dynamic forces (e.g., traffic-induced excitations). These bridges show a characteristic nonlinear precritical behavior under quasistatic incremental loads and, depending on the direction of loading (downward or upward), the ensuing increase or loss of tension in the suspension cables causes an increase or a loss of stiffness as a result of the positive or negative geometric stiffness effects, respectively. Thus, to predict correctly any static or dynamic critical condition, it is necessary to describe accurately the overall precritical behavior as well as the mechanical asymmetry exhibited by these formidable suspended structures. Moreover, phenomena such as the static and dynamic aeroelastic instabilities induced by wind-structure interaction can be investigated effectively only in the context of a parametric modeling and a continuum formulation of the elastostatic and elastodynamic problems.

Several numerical models of suspension bridges have been proposed in the technical literature and different studies have been conducted to investigate their static/dynamic response and the aeroelastic limit states. One of the first and most important contributions can be found in [1] where parametric formulations are adopted to describe the static and dynamic response of cables and suspended structures. Different studies on linearized models of suspension bridges can be found in [2–5], whereas the first general theory and analysis of nonlinear vibrations of such structures are proposed in [6, 7] where the authors used the method of multiple scales to investigate nonlinear free flexural-torsional vibrations. By the same method, passive and active schemes were investigated to control nonlinear oscillations in suspension bridges [8, 9]. Most recent works can be found in [10] and in [11, 12] in which the nonlinear equations of motion are obtained by employing variational methods based on truncated geometric nonlinearities.

The model proposed here accounts for the elastic characteristics of the suspension hangers, modeled as a continuum elastic (membrane-type) distribution along the bridge span while the Cosserat theory is employed to describe the mechanics of the deck-girder. No restrictions are placed on the geometry

of deformation besides the rigidity of the cross sections. The equations of motion are thus derived via a Lagrangian formulation which allows to include in a straightforward manner nonconservative loads such as aeroelastic forces. Studies on the static aeroelastic instability of long-span cable-stayed bridges were carried out in [13] to evaluate the critical wind velocity for the nonlinear lateral-torsional buckling instability via a Finite Element (FE) approach. Three-dimensional nonlinear FE analyses on a super-long-span suspension bridge were also performed in [14] to demonstrate the significant influence of the geometric nonlinearities on the aerostatic and aerodynamic behaviors of such slender structures. In [15, 16], a series method was proposed for the deterministic aerostatic stability analysis of suspension bridges; however, some conservative assumptions in the kinematic modeling and in the prestress contribution of the dead and wind-induced loads were made. In [17], numerical aerostatic stability analyses are performed on a three-dimensional FE model of a suspension bridge to study the combined effects of geometric and material nonlinearities and the nonlinear modeling of the wind loads. A simplified method to analyze the lateral response of suspension bridges under wind loads was proposed by [18] deriving the analytical formulas of the aeroelastic response for a three degrees of freedom (dof) model under some kinematic and mechanical assumptions. A continuum model of suspension bridges that can undergo three-dimensional motions, was first proposed in [19, 20]. The model was formulated via a total Lagrangian approach within a geometrically exact framework. The torsional divergence condition was determined as the static bifurcation condition whence the tangent stiffness along the nonlinear equilibrium path becomes singular while increasing the wind speed. The dynamic aeroelastic behavior of suspension bridges has also been widely investigated in the literature by different numerical strategies. The flutter instability, whose general theory is given in [21], is classically studied by two approaches, namely, the frequency- and time-domain approaches [22]. The importance of the structural nonlinearities on the aerodynamic response of suspension bridges is a well-known fact as shown in [23].

In [24], the concept of aeroelastic derivatives (see also [25] and [26]) was first proposed to evaluate the flutter wind speed by solving a complex-valued eigen-

value problem whose solution represents the bridge frequency at the flutter condition. A modal analysis technique was applied in [27–29], and more recently in [30] and [31] for the evaluation of the critical flutter speed of a suspension bridge by using a linear three-dimensional multi-dof framework. A numerical model that treats the bridge and flowing air as elements of a single dynamic system was proposed in [32] where the governing equations are integrated numerically, simultaneously, and interactively to predict the onset of flutter.

The correct evaluation of the bridge tangent stiffness in the prestressed configuration induced by the in-service loads, accounting also for the torsional and out-of-plane components, is a necessary step within the context of an accurate study of the limit states arising from wind-structure interaction. In bridge design, aeroelastic phenomena are usually investigated in the context of cumbersome FE models where sensitivity parametric analyses are computationally demanding because the regeneration of the mesh for the whole geometry of the bridge must be carried out for each individual analysis. On the other hand, the proposed geometrically exact continuum model of suspension bridges represents a suitable parametric framework for investigating limit states and conducting rapid structural optimization studies.

A fully nonlinear parametric model for the study of wind-induced excitation in arch bridges was first proposed in [33] and [34] where the flutter analysis of Ponte della Musica, recently constructed in Rome, was carried out by solving the complex eigenvalue problem associated with the governing equations of motion linearized about the in-service prestressed bridge configuration under dead loads and wind-induced forces. The same approach was followed in [35] on a classical FE model. An interesting application of classical eigenvalue analysis for the critical flutter condition on a real bridge is given in [36] and [37] where an iterative procedure was employed to estimate the flutter velocity for different angles of attack of the wind and several suspension bridge configurations. In [38], a FE calculation of the aerodynamic flutter phenomenon is presented for a cable-stayed bridge by solving the eigenvalue problem delivered by the mode-by-mode method with the limitation that it neglects a priori any modal coupling. A multimode flutter analysis was performed in [39] by a FE model. To account for the spatial distribution of the wind force

field, especially for long-span bridges, some authors [40, 41] proposed a three-dimensional flutter analysis of a simply supported bridge girder by the so-called finite strip method, which allows to consider distributed wind forces on different strips of the bridge girder.

To perform aeroelastic stability studies, an alternative strategy is the analysis in the time-domain where the bridge response is carried out within a given range of wind speeds that is expected to bracket the flutter speed [42] and the critical condition is found when the bridge dynamic response shows a periodic oscillation. With respect to the eigenvalue approach, time-domain analyses allow to study the post-critical flutter response with the structural and aerodynamic nonlinearities [43, 44]. The drawbacks are the high computational burden and the high computational complexity necessary to obtain appropriate analytical functions for typical cross-sections of a deck bridge. The aerodynamic forces acting on the bridge deck are usually modeled relying on the so-called aeroelastic derivatives, which correspond to a set of functions evaluated through wind-tunnel tests on a sectional scaled model of the reference bridge [26, 45, 46].

The main contribution of the present work is to provide a geometrically exact one-dimensional formulation of the static and dynamic aeroelastic problem for suspension bridges and validate the aeroelastic predictions based on this model. The fairly general modeling allows to take into account accurately any nonuniform stiffness and mass properties as well as all other nonuniform data (e.g., the wind force distribution), as demonstrated in [34, 47]. The static aeroelastic stability of two suspension bridges is then investigated by performing nonlinear incremental analyses and evaluating the critical, torsional-divergence. The flutter analysis is then formulated for one case study, the Runyang suspension bridge, and a comparison between two modal techniques is proposed; the study is in fact conducted by performing a complex-valued eigenvalue problem and a classical, iterative, eigenvalue problem by considering the prestressed configurations induced by the bridge dead loads and the in-service loads as well as the static components of the wind loads. A few sensitivity analyses are then carried out in order to demonstrate the wide applicability of the model.

2 The one-dimensional model of suspension bridges

A three-dimensional geometrically exact approach [48] is employed to obtain the equations of motion according to a Total and an updated Lagrangian formulation. The bridge undeformed (stress-free) configuration is considered as the reference configuration. The fixed Cartesian reference frame $\{e_1, e_2, e_3\}$ has the origin in the center of mass of the left deck terminal section (see Fig. 1). For the two suspension cables under their own weight, the catenary equilibrium configurations, taken as reference configuration, are given by

$$y^c(x) = \frac{H^c}{\rho A^c g} \left\{ \cosh \left[\frac{\rho A^c g}{H^c} \left(\frac{l}{2} - x \right) \right] - \cosh \frac{\rho A^c g l}{2H^c} \right\}, \tag{1}$$

where x is the horizontal coordinate along the base line of the deck in the reference configuration (here, it is taken to coincide with the centerline), ρA^c is the cable mass per unit length, g is the gravitational constant, l is the span of the bridge, and H^c is the horizontal component of the tension N^c in each cable. To identify the two suspension cables and the associated variables, the superscripts “+” and “-” are introduced with the convention that the plus sign refers to the cable undergoing incremental tension, the minus indicates the cable undergoing tension loosening, respectively, when the deck is subject to a counter-

clockwise rotation. The orientation of the deck cross section in the reference configuration is given by the unit vectors $\{b_1(x), b_2(x)\}$ collinear with the principal inertia directions. The local frame is completed by the unit vector $b_3 = b_1 \times b_2$ orthogonal to the cross section. For the suspension cables in the reference configuration, the unit vectors $a_3^\pm(x)$ represent the local tangent to the cable base lines (i.e., the cables centerlines). To complete the local frame for the cables, a pair of orthogonal unit vectors $\{a_1^\pm(x), a_2^\pm(x)\}$ lying in the plane orthogonal to $a_3^\pm(x)$ is considered.

Kinematic and dynamic formulation In the orthonormal basis of the fixed inertial reference frame $\{e_1, e_2, e_3\}$, the reference (stress-free) configuration of the deck is described by the position vector of the centerline, $x(x) = x e_3$, where x is the coordinate along the bridge span (see Fig. 1); on the other hand, the reference configurations of the two cables are given by the vectors $y^\pm(x)$. The equilibrium configurations of the deck-girder and cables under the static loads, respectively, denoted by B_o and C_o , are described by

$$p_o = x(x) + u_o(x), \quad q_o^\pm = y^\pm(x) + v_o^\pm(x). \tag{2}$$

The orientation of the deck cross sections is given by unit vectors $\{b_1^o(x), b_2^o(x), b_3^o(x)\}$, whereas the cables tangent unit vectors are $a_\alpha^\pm(x)$, where the subscript 3 is omitted for ease of notation. In terms of the

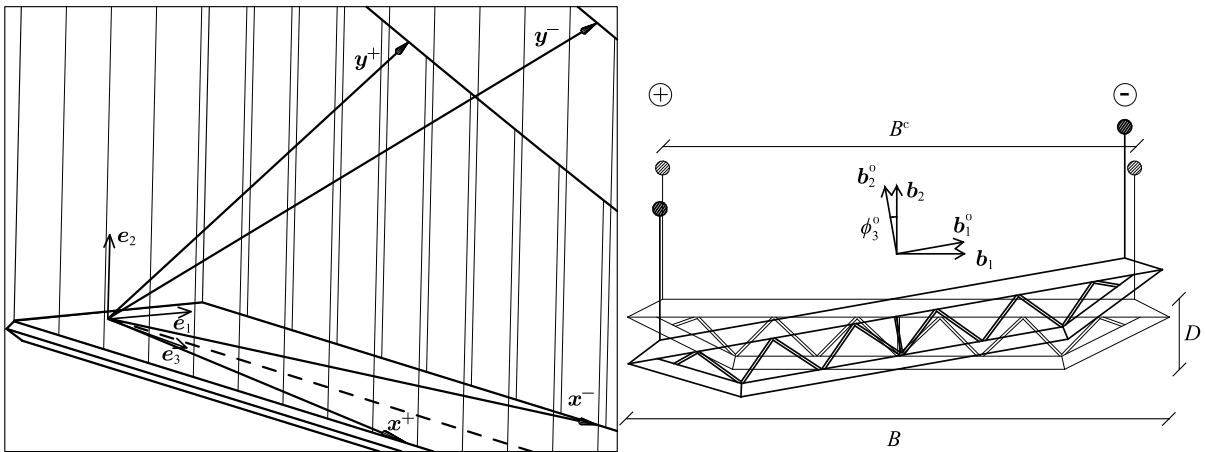


Fig. 1 Three-dimensional view (left) and deck section reference frames (right) of the suspension bridge model

fixed basis $\{\mathbf{e}_1, \mathbf{e}_2, \mathbf{e}_3\}$, they are expressed as

$$\begin{aligned} \mathbf{b}_i^0(x) &= \sum_{j=1}^3 R_{j,i}^0(x) \mathbf{e}_j, \\ \mathbf{a}_0^\pm(x, t) &= \frac{\cos \theta^c}{v_0^\pm} [v_{0,1,x}^\pm \mathbf{e}_1 \\ &\quad + (y_x^c + v_{0,2,x}^\pm) \mathbf{e}_2 + (1 + v_{0,3,x}^\pm) \mathbf{e}_3], \end{aligned} \tag{3}$$

where $\cos \theta^c$ is the horizontal projection of the tangent unit vector to the catenary cable configuration $y^c(x)$, $\theta^c = \arctan(y_x^c(x))$, the subscript x indicates differentiation with respect to x and $R_{j,i}^0(x)$ represents the (j, i) th component of the orthogonal matrix \mathbf{R}^0 obtained through the following sequence of finite rotations: flexural rotation about axis \mathbf{e}_1 , flexural rotation about $\mathbf{b}_2^{(1)}$ and torsional rotation about axis $\mathbf{b}_3^{(2)}$ where $\{\mathbf{b}_1^{(k)}, \mathbf{b}_2^{(k)}, \mathbf{b}_3^{(k)}\}$ is the basis resulting from the k th rotation. The components of \mathbf{R}^0 are given in the Appendix.

The motions of base lines of the deck-girder and the cables, respectively, are described by $\check{\mathbf{p}}(x, t)$ and $\check{\mathbf{q}}^\pm(x, t)$:

$$\begin{aligned} \check{\mathbf{p}}(x, t) &= \mathbf{p}_0(x) + \mathbf{u}(x, t), \\ \check{\mathbf{q}}^\pm(x, t) &= \mathbf{q}_0^\pm(x) + \mathbf{v}^\pm(x, t). \end{aligned} \tag{4}$$

The deck intrinsic frame $\{\check{\mathbf{b}}_1(x, t), \check{\mathbf{b}}_2(x, t), \check{\mathbf{b}}_3(x, t)\}$ and the cables tangent unit vectors $\check{\mathbf{a}}_3^\pm(x, t)$ can be expressed in terms of the fixed basis $\{\mathbf{e}_1, \mathbf{e}_2, \mathbf{e}_3\}$ as

$$\begin{aligned} \check{\mathbf{b}}_i(x, t) &= \sum_{j=1}^3 \check{R}_{j,i}(x, t) \mathbf{e}_j, \\ \check{\mathbf{a}}^\pm(x, t) &= \frac{\cos \theta^c}{\check{v}^\pm} [(v_{0,1,x}^\pm + v_{1,x}^\pm) \mathbf{e}_1 \\ &\quad + (y_x^c + v_{0,2,x}^\pm + v_{2,x}^\pm) \mathbf{e}_2 \\ &\quad + (1 + v_{0,3,x}^\pm + v_{3,x}^\pm) \mathbf{e}_3], \end{aligned} \tag{5}$$

where $\check{R}_{j,i}(x, t)$ is the component of the total rotation matrix $\check{\mathbf{R}}(x, t)$ obtained as

$$\check{\mathbf{R}}(x, t) := \mathbf{R}^0(x) \cdot \mathbf{R}(x, t). \tag{6}$$

In Eq. (6), $\mathbf{R}(x, t)$ represents the sequence of incremental finite rotations $\phi_i(x, t)$ from the static configuration \mathcal{B}_0 to the dynamic configuration $\check{\mathcal{B}}$ and its components are formally the same as those shown in (28).

The generalized total strain parameters are defined in the local basis of each structural element. For the cables, the static stretch and the total dynamic stretch are given by

$$v_0^\pm = \partial_{s^c} \mathbf{q}_0^\pm \cdot \mathbf{a}_0^\pm, \quad \check{v}^\pm = \partial_{s^c} \check{\mathbf{q}}^\pm \cdot \check{\mathbf{a}}^\pm, \tag{7}$$

where $\partial_s(\cdot)$ indicates the derivative with respect to the cable arc length coordinate s^c , $\partial_{s^c}(\cdot) = \cos \theta^c \partial_x(\cdot)$ and $\partial_x(\cdot)$ indicates differentiation with respect to the bridge span coordinate x . The deck generalized strains comprise the stretch, the two shear strains, the two bending curvatures, and the twist curvature defined as

$$\begin{aligned} \partial_x \mathbf{p}_0 &= \eta_1^0 \mathbf{b}_1^0 + \eta_2^0 \mathbf{b}_2^0 + v^0 \mathbf{b}_3^0, & \partial_x \mathbf{b}_k^0 &= \boldsymbol{\mu}^0 \times \mathbf{b}_k^0, \\ \partial_x \check{\mathbf{p}} &= \check{\eta}_1 \check{\mathbf{b}}_1 + \check{\eta}_2 \check{\mathbf{b}}_2 + \check{v} \check{\mathbf{b}}_3, & \partial_x \check{\mathbf{b}}_k &= \check{\boldsymbol{\mu}} \times \check{\mathbf{b}}_k. \end{aligned} \tag{8}$$

For the equilibrium and dynamic configurations \mathcal{B}^0 and $\check{\mathcal{B}}$, v^0 and \check{v} represent the deck stretches, (η_1^0, η_2^0) and $(\check{\eta}_1, \check{\eta}_2)$ are the shear strains along the \mathbf{b}_1^0 and \mathbf{b}_2^0 and $\check{\mathbf{b}}_1$ and $\check{\mathbf{b}}_2$ directions, respectively. The components of the curvature vector in the static and dynamic local basis ($\boldsymbol{\mu}^0 = \mu_1^0 \mathbf{b}_1^0 + \mu_2^0 \mathbf{b}_2^0 + \mu_3^0 \mathbf{b}_3^0$, $\check{\boldsymbol{\mu}} = \check{\mu}_1 \check{\mathbf{b}}_1 + \check{\mu}_2 \check{\mathbf{b}}_2 + \check{\mu}_3 \check{\mathbf{b}}_3$) denote the torsional curvatures ($\mu_3^0, \check{\mu}_3$) and the bending curvatures ($\mu_1^0, \check{\mu}_1$) and ($\mu_2^0, \check{\mu}_2$), respectively.

To describe the cables equilibrium and dynamic contact forces, vectors \mathbf{n}_0^\pm and $\check{\mathbf{n}}^\pm$ are introduced

$$\mathbf{n}_0^\pm(x) = N_0^\pm(x) \mathbf{a}_0^\pm, \quad \check{\mathbf{n}}^\pm(x, t) = \check{N}^\pm(x, t) \check{\mathbf{a}}^\pm. \tag{9}$$

The generalized stress resultants and stress moment resultants of the deck-girder are given by $(\mathbf{n}^0, \mathbf{m}^0)$ in \mathcal{B}^0 and by $(\check{\mathbf{n}}, \check{\mathbf{m}})$ in $\check{\mathcal{B}}$. The component form of the deck contact forces and couples is given by

$$\begin{aligned} \mathbf{n}^0(x) &= Q_1^0(x) \mathbf{b}_1^0 + Q_2^0(x) \mathbf{b}_2^0 + N^0(x) \mathbf{b}_3^0, \\ \check{\mathbf{n}}(x, t) &= \check{Q}_1(x, t) \check{\mathbf{b}}_1 + \check{Q}_2(x, t) \check{\mathbf{b}}_2 + \check{N}(x, t) \check{\mathbf{b}}_3, \\ \mathbf{m}^0(x) &= M_1^0(x) \mathbf{b}_1^0 + M_2^0(x) \mathbf{b}_2^0 + T^0(x) \mathbf{b}_3^0, \\ \check{\mathbf{m}}(x, t) &= \check{M}_1(x, t) \check{\mathbf{b}}_1 + \check{M}_2(x, t) \check{\mathbf{b}}_2 + \check{T}(x, t) \check{\mathbf{b}}_3, \end{aligned} \tag{10}$$

where the components have the meaning of tensions (N^0, \check{N}), shear forces (Q_1^0, \check{Q}_1) and (Q_2^0, \check{Q}_2) for the contact force vectors $(\mathbf{n}^0, \check{\mathbf{n}})$ while, for the contact couples $(\mathbf{m}^0, \check{\mathbf{m}})$, they represent the torques (T^0, \check{T})

and the bending moments (M_1^0, \check{M}_1) and (M_2^0, \check{M}_2) . The equilibrium equations can thus be written as

$$\begin{aligned} \partial_x \mathbf{n}_0^\pm + \mathbf{f}_0^\pm - \mathbf{r}_0^\pm &= \mathbf{o}, \\ \partial_x \mathbf{n}^0 + \mathbf{f}^0 + \mathbf{r}_0^+ + \mathbf{r}_0^- &= \mathbf{o}, \\ \partial_x \mathbf{m}^0 + \partial_x \mathbf{p}_0 \times \mathbf{n}^0 + \frac{B^c}{2} \mathbf{b}_1^c \times (\mathbf{r}_0^- - \mathbf{r}_0^+) + \mathbf{c}^0 &= \mathbf{o}, \end{aligned} \tag{11}$$

where the forces $\mathbf{f}_0^\pm(x)$, $\mathbf{f}^0(x)$ and couples $\mathbf{c}^0(x)$ include the cables and deck weights and B^c represents the distance between the two suspension cables (see Fig. 1).

The equations of motion are obtained by enforcing the balance of linear and angular momentum for the cable-deck system. The equations of motion read

$$\begin{aligned} \partial_x \check{\mathbf{n}}^\pm + \check{\mathbf{f}}^\pm - \check{\mathbf{r}}^\pm &= \rho A^c \sec \theta_0^\pm(x) \partial_{tt} \mathbf{v}^\pm, \\ \partial_x \check{\mathbf{n}} + \check{\mathbf{f}} + \check{\mathbf{r}}^+ + \check{\mathbf{r}}^- &= \rho A^d \partial_{tt} \mathbf{u}, \\ \partial_x \check{\mathbf{m}} + \partial_x \check{\mathbf{p}} \times \check{\mathbf{n}} + \frac{B^c}{2} \check{\mathbf{b}}_1 \times (\check{\mathbf{r}}^- - \check{\mathbf{r}}^+) + \check{\mathbf{c}} &= \rho \mathbf{J}^E \cdot \partial_t \boldsymbol{\omega} + \boldsymbol{\omega} \times (\rho \mathbf{J}^E \cdot \boldsymbol{\omega}), \end{aligned} \tag{12}$$

where $\partial_t(\cdot)$ indicates partial differentiation with respect to time t and $\sec \theta_0^\pm(x) = v_0^\pm / [\cos \theta^c (1 + \partial_x v_{03}^\pm)]$; ρA^c and ρA^d are the cables and deck mass per unit length, respectively, $\rho \mathbf{J}^E$ is the tensor of the inertia mass moments of the deck cross sections referred to the elastic center C^E (here, it coincides with the center of mass); $\boldsymbol{\omega}(x, t)$ is the incremental angular velocity vector of the cross sections defined in the local reference frame such that $\partial_t \check{\mathbf{b}}_k = \boldsymbol{\omega}(x, t) \times \check{\mathbf{b}}_k$. In addition, $\check{\mathbf{f}}(x, t)$ and $\check{\mathbf{c}}(x, t)$ denote the total forces and couples per unit length, respectively, acting in the deck current dynamic configuration and include the damping forces which are assumed proportional to the velocity $\partial_t \mathbf{u}$ and the angular velocity $\boldsymbol{\omega}(x, t)$. Linearly elastic constitutive laws are assumed in order to describe the relations between the generalized stress resultant forces and couples and the generalized strain parameters.

The hangers strain and the tension \mathbf{r}_0^\pm and $\check{\mathbf{r}}^\pm$ can be defined assuming an equivalent continuous hangers distribution along the bridge span; accordingly $l_h(x) := h + y^c(x)$ is a function that defines the hangers undeformed length along the bridge span and h is the height of the bridge towers measured from the deck. The cables catenaries can be described in the fixed frame by $\mathbf{y}^\pm(x) = \mp (B^c/2) \mathbf{e}_1 + l_h(x) \mathbf{e}_2 + x \mathbf{e}_3$.

The expressions of the static and dynamic hanger stretches $v_h^{0\pm}(x)$ and $\check{v}_h^\pm(x, t)$ are obtained as

$$v_h^{0\pm}(x) = \frac{\|\mathbf{q}_0^\pm - \mathbf{p}_0^\pm\|}{l_h(x)}, \quad \check{v}_h^\pm(x, t) = \frac{\|\check{\mathbf{q}}^\pm - \check{\mathbf{p}}^\pm\|}{l_h(x)}. \tag{13}$$

The vectors \mathbf{p}_0^\pm and $\check{\mathbf{p}}^\pm$ indicate the position vectors of the hanger points of attachment onto the deck in the static and dynamic configurations, respectively, and their expressions are given by

$$\begin{aligned} \mathbf{p}_0^\pm(x) &= \mathbf{x}_o(x) + \mathbf{u}_0^\pm(x), \\ \check{\mathbf{p}}^\pm(x, t) &= \mathbf{x}_o(x) + \check{\mathbf{u}}^\pm(x, t), \\ \mathbf{u}_0^\pm(x) &= \mathbf{u}_o(x) \mp \frac{B^c}{2} (\mathbf{b}_1^o(x) - \mathbf{e}_1), \\ \check{\mathbf{u}}^\pm(x, t) &= \check{\mathbf{u}}(x, t) \mp \frac{B^c}{2} (\check{\mathbf{b}}_1(x, t) - \mathbf{e}_1), \end{aligned} \tag{14}$$

where, the total displacement of the deck and cable base lines, $\check{\mathbf{u}}(x, t)$ and $\check{\mathbf{v}}^\pm(x, t)$, respectively, are defined as

$$\begin{aligned} \check{\mathbf{u}}(x, t) &:= \mathbf{u}_o(x) + \mathbf{u}(x, t), \\ \check{\mathbf{v}}^\pm(x, t) &:= \mathbf{v}_0^\pm(x) + \mathbf{v}^\pm(x, t). \end{aligned} \tag{15}$$

The elastic constitutive law for the hangers can be written as

$$\begin{aligned} \mathbf{r}_0^\pm(x) &= \frac{E^h A^h}{l_h(x)} (v_h^{0\pm}(x) - 1) \mathbf{e}_{oh}^\pm, \\ \check{\mathbf{r}}^\pm(x, t) &= \frac{E^h A^h}{v_h^{0\pm}(x) l_h(x)} (\check{v}_h^\pm(x, t) - 1) \check{\mathbf{e}}_h^\pm, \\ \mathbf{e}_{oh}^\pm &= \frac{\mathbf{q}_0^\pm - \mathbf{p}_0^\pm}{\|\mathbf{q}_0^\pm - \mathbf{p}_0^\pm\|}, \\ \check{\mathbf{e}}_h^\pm &= \frac{\check{\mathbf{q}}^\pm - \check{\mathbf{p}}^\pm}{\|\check{\mathbf{q}}^\pm - \check{\mathbf{p}}^\pm\|}. \end{aligned} \tag{16}$$

Finally, the kinematic and mechanical boundary conditions are referred to a simply-supported scheme for the deck while the two suspension cables ends are fixed atop the towers. They can be written in the global reference frame $\{\mathbf{e}_1, \mathbf{e}_2, \mathbf{e}_3\}$ as

$$\begin{aligned} \mathbf{u}_o(0) &= \mathbf{o}, & \mathbf{m}^o(0) \cdot \mathbf{e}_1 &= 0, \\ \psi_2^o(0) &= 0, & \psi_3^o(0) &= 0, & \mathbf{u}_o(l) \cdot \mathbf{e}_1 &= 0, \\ \mathbf{u}_o(l) \cdot \mathbf{e}_2 &= 0, & \mathbf{n}^o(l) \cdot \mathbf{e}_3 &= 0, \end{aligned}$$

$$\begin{aligned}
 \mathbf{m}^o(l) \cdot \mathbf{e}_1 &= 0, & \psi_2^o(l) &= 0, & \psi_3^o(l) &= 0, \\
 \mathbf{v}_0^\pm(0) &= \mathbf{o}, & \mathbf{v}_0^\pm(l) &= \mathbf{o}, \\
 \check{\mathbf{u}}(0, t) &= \mathbf{o}, & \check{\mathbf{m}}(0, t) \cdot \mathbf{e}_1 &= 0, \\
 \check{\psi}_2(0, t) &= 0, & \check{\psi}_3(0, t) &= 0, \\
 \check{\mathbf{u}}(l, t) \cdot \mathbf{e}_1 &= 0, & \check{\mathbf{u}}(l, t) \cdot \mathbf{e}_2 &= 0, \\
 \check{\mathbf{n}}(l, t) \cdot \mathbf{e}_3 &= 0, & \check{\mathbf{m}}(l, t) \cdot \mathbf{e}_1 &= 0, \\
 \check{\psi}_2(l, t) &= 0, & \check{\psi}_3(l, t) &= 0,
 \end{aligned} \tag{17}$$

where $\psi_i^o(x)$ and $\check{\psi}_i(x, t)$, $i = 1, 2, 3$, represent the static and dynamic rotations of the deck cross-section and their expressions are given in the [Appendix](#).

Nondimensional form The governing static and dynamic equations (11) and (12), and the associated boundary conditions (17), are cast in nondimensional form by using the deck span l as characteristic length and $\sqrt{\rho A^d l^4 / E^d J_1}$ as characteristic time, where ρA^d is the deck mass per unit length, E^d is the deck Young modulus and J_1 the moment of inertia about the local axis \mathbf{b}_1 . The deck nondimensional mass per unit length turns out to be $\varrho^d = 1$ whereas the cables mass in nondimensional form can be written as $\varrho^c = \rho A^c / \rho A^d$. Moreover, the nondimensional structural damping coefficients are expressed as

$$D_j^c = 2\zeta \omega_j \varrho^c, \quad D_j^d = 2\zeta \omega_j, \quad D_j^T = 2\zeta \omega_j \bar{J}^m, \tag{18}$$

where ζ is the damping ratio and ω_j is the nondimensional natural frequency of the j th natural vibrational mode of the bridge; $\bar{J}^m = (\rho J_3^E + \frac{1}{2} \rho A^c B^c) / (\rho A^d l^2)$ is the nondimensional mass moment along the direction $\check{\mathbf{b}}_3$ of the deck accounting for the cables mass contribution. The contribution of the flexural angular rates on the structural damping is neglected. The independent nondimensional stiffness parameters are defined as ratios to the flexural deck stiffness $E^d J_1 / l^3$.

The nondimensionalized equations (11) and (12), projected into the fixed basis $\{\mathbf{e}_1, \mathbf{e}_2, \mathbf{e}_3\}$, yield twelve nonlinear partial-differential equations in twelve independent kinematic unknowns. The obtained equations govern the elasto-static and elastodynamic problems, respectively, and the following independent parameters are introduced to cast the model in nondimen-

sional form:

$$\begin{aligned}
 \alpha^c &= \frac{H^c l^2}{E^d J_1}, & \kappa^c &= \frac{E^c A^c l^2}{E^d J_1}, \\
 \kappa^h &= \frac{E^h A^h l^2}{E^d J_1}, & \kappa^d &= \frac{A^d l^2}{J_1}, \\
 \gamma_j &= \frac{G^d A_j^{*d} l^2}{E^d J_1}, & \chi &= \frac{J_2}{J_1}, & \tau &= \frac{G^d J_3}{E^d J_1},
 \end{aligned} \tag{19}$$

where A^c and A^h are the cables and hangers cross-section area, E^c and E^h their Young modulus, A^d and A^{*d} are the deck cross-section area and shear area in direction \mathbf{b}_j , $j = 1, 2$, G^d is the shear modulus; J_2 and J_3 are the flexural moment of inertia and the torsional moment of inertia. The space and time nondimensional coordinates are then defined as $x = l\bar{x}$, $y^c(x) = l\bar{y}^c(\bar{x})$, $y^\pm(x) = l\bar{y}^\pm(\bar{x})$, $t = \bar{t}/\bar{\omega}$, $\bar{\omega} = \sqrt{E^d J_1 / (\rho A^d l^4)}$ and the displacement vectors as $\mathbf{u} = l\bar{\mathbf{u}}$, $\mathbf{v}^\pm = l\bar{\mathbf{v}}^\pm$. Accordingly, by considering the definitions in (19), the elastic constitutive laws can be expressed in the nondimensional form:

$$\begin{aligned}
 N_0^\pm &= N^c + \kappa^c (v_0^\pm - 1), & N^o &= \kappa^d (v^o - 1), \\
 Q_1^o &= \gamma_1 \eta_1^o, & Q_2^o &= \gamma_2 \eta_2^o, \\
 M_1^o &= \mu_1^o, & M_2^o &= \chi \mu_2^o, & T^o &= \tau \mu_3^o, \\
 \check{N}^\pm &= N^c + \kappa^c (\check{v}^\pm - 1), & \check{N} &= \kappa^d (\check{v} - 1), \\
 \check{Q}_1 &= \gamma_1 \check{\eta}_1, & \check{Q}_2 &= \gamma_2 \check{\eta}_2, \\
 \check{M}_1 &= \check{\mu}_1, & \check{M}_2 &= \chi \check{\mu}_2, & \check{T} &= \tau \check{\mu}_3, \\
 \mathbf{r}_0^\pm(x) &= \frac{\kappa^h}{l_h(x)} (v_h^{o\pm}(x) - 1) \mathbf{e}_{0h}^\pm, \\
 \check{\mathbf{r}}^\pm(x, t) &= \frac{\kappa^h}{v_h^{o\pm}(x) l_h(x)} (\check{v}_h^\pm(x, t) - 1) \check{\mathbf{e}}_h^\pm,
 \end{aligned} \tag{20}$$

where $N^c = \alpha^c / \cos \theta^c$ is the catenary cable tension and $\bar{l}_h = l_h / l$.

3 Computational approach

The coupled nonlinear partial-differential equations of motion (12), cast in a nondimensional form, are implemented in the computational platform [49] using the PDE-mode feature. The space-time integration is numerically performed by using the FE method. The mesh of one-dimensional domain $[0, 1]$ was adapted to

optimize the accuracy and evaluation time of the solution. Fourth-order Lagrangian polynomials were used to approximate each of the 12 kinematic independent variables of the system.

3.1 Model validation

A preliminary validation of the equations of motion is performed evaluating the modal properties of two existing suspension bridges: the Runyang Suspension Bridge with a span of 1490 m and the Hu Men Suspension Bridge having a span of about 888 m. These two bridges have more or less the same shape and cross-sectional size, but a very different span since the Runyang span is about 70 % greater than the Hu Men span. This implies significantly different nonlinear behaviors as highlighted by the investigations carried out in this work about the static aeroelastic stability. The following analyses are based on the reference mechanical parameters and the obtained results are compared with those proposed in [14, 36, 37] for the Runyang bridge and [15, 18] for the Hu Men bridge, respectively.

The elastogeometric properties of the girder-deck of the Runyang and Hu Men bridges can be summarized as follows: $l = 1490/888$ m, $B = 35.9/35.6$ m, $D = 3/3.012$ m, $A^d = 1.2481/1.2443$ m², $\rho A^d = 18387/18330$ kg/m, $\rho J_3^E = 1.852 \times 10^6/1.743 \times 10^6$ kg m²/m, $E = 210/210$ GPa, $G = 80.77/80.77$ GPa, $J_1 = 1.9842/1.98$ m⁴, $J_2 = 137.7541/124.39$ m⁴, $J_3^E = 5.034/5.1$ m⁴. Here and henceforth, the slash separates quantities referred to the Runyang bridge (left of the slash) from those referred to the Hu Men bridge (right of the slash). On the other hand,

the suspension cables exhibit the following properties: $E^c = 200/200$ GPa, $d^c = 0.776/0.623$ m, $A^c = 0.47347/0.305$ m², $\rho A^c = 3817/2397$ kg/m. The sag of the cables under their own weight is 149/84.6 m and the horizontal force is $H^c = 7.09626/2.792 \times 10^7$ N. The hangers have the following properties: $E^h = 210/160$ GPa, $d^h = 0.0522/0.0529$ m, $A^h = 2.14/2.198 \times 10^{-3}$ m², and the distance between the hangers is $B^c = 34.3/33$ m. The height of the towers is $h = 154/90$ m. The damping factor is 0.5 % for both bridges.

The eigenvalue problem is solved considering the bridge deformed configuration under dead loads so as to account for the prestressed state. The study is performed in two steps: in the first step, the equilibrium equations (11) are solved to obtain the equilibrium state and the generalized stresses are evaluated across the structure. In the second step, the lowest natural frequencies and mode shapes of the bridge are evaluated solving the eigenvalue problem associated with Eqs. (12) including the computed equilibrium configuration.

In Table 1 the lowest few frequencies of the bridge modes are illustrated and compared with the literature results obtained via a linear FE model of the structure. Slightly higher values obtained by the proposed model are due to the adopted continuum formulation in which the stiffness parameters are average values and the real discrete hanger distribution is replaced by a continuum equivalent distribution. The kinematic unknowns, which govern such a rich mechanical problem in the present continuum formulation, are only 12.

Table 1 Frequencies of the lowest six modes of the Runyang suspension bridge about the stress-free and prestressed configurations. SF stands for stress-free and PS refers to pre-stresses

condition, whereas $F-1$, $F-2$, and T identify the flexural modes in directions e_2 and e_3 and the torsional mode, respectively

		Proposed parametric nonlinear model						
		f_1 [Hz]	f_2 [Hz]	f_3 [Hz]	f_4 [Hz]	f_5 [Hz]	f_6 [Hz]	f_7 [Hz]
		$F-1$ sym	$F-2$ skew	$F-2$ sym	$F-1$ skew	$F-2$ skew	T skew	T sym
		$v_1^\pm u_1$	v_2^\pm, u_2	v_2^\pm, u_2	$v_1^\pm u_1$	v_2^\pm, u_2	v_2^\pm, ϕ_3	v_2^\pm, ϕ_3
SF		0.045 0.064	0.050	0.074	0.09 0.175	0.108	0.211	0.253
		v_1^\pm, u_1	v_2^\pm, u_2	v_2^\pm, u_2	v_1^\pm, u_1	v_2^\pm, u_2	v_2^\pm, ϕ_3	$\check{v}_2^\pm, \check{\phi}_3$
PS		0.070	0.096	0.128	0.1707	0.1797	0.229	0.277
Literature results [36]				0.126		0.172		0.241

Table 2 Frequencies of the lowest six modes of the *Hu Men* suspension bridge about the stress-free and pre-stressed configurations. *SF* stands for stress-free and *PS* refers to pre-stresses

condition, whereas *F-1*, *F-2* and *T* identify the flexural modes in directions e_2 and e_3 and the torsional mode, respectively

	Proposed parametric nonlinear model						
	f_1 [Hz]	f_2 [Hz]	f_3 [Hz]	f_4 [Hz]	f_5 [Hz]	f_6 [Hz]	f_7 [Hz]
	<i>F-1 sym</i>	<i>F-2 skew</i>	<i>F-2 sym</i>	<i>F-1 skew</i>	<i>F-2 skew</i>	<i>T skew</i>	<i>T sym</i>
	$v_1^\pm u_1$	v_2^\pm, u_2	v_2^\pm, u_2	$v_1^\pm u_1$	v_2^\pm, u_2	v_2^\pm, ϕ_3	v_2^\pm, ϕ_3
<i>SF</i>	0.06 0.170	0.065	0.106	0.119 0.469	0.174	0.402	0.409
	<i>F-2 skew</i>	<i>F-1 sym</i>	<i>F-2 sym</i>	<i>F-2 skew</i>	<i>F-1 skew</i>	<i>T skew</i>	<i>T sym</i>
	v_2^\pm, u_2	v_1^\pm, u_1	v_2^\pm, u_2	v_2^\pm, u_2	v_1^\pm, u_1	v_2^\pm, ϕ_3	v_2^\pm, ϕ_3
<i>PS</i>	0.129	0.161	0.181	0.269	0.319	0.434	0.439
Literature results [35]	–	–	0.172	–	–	0.426	0.361

The first row gives the frequencies calculated considering the stress-free configuration of the bridge. The first mode is a symmetric local mode affecting the cables alone moving in the out-of-plane direction in a pendulum-like mode. The second mode is the first symmetric lateral bending mode for the deck involving also the cables. The modes that follow in the sequence are the lowest skew-symmetric and lowest symmetric bending modes in the vertical direction. Thereafter, the bridge exhibits the lowest skew-symmetric lateral mode and the second skew-symmetric mode in the vertical direction. The sixth and the seventh modes are the lowest skew-symmetric and symmetric torsional modes.

On the other hand, if the prestressed condition is taken into account, the local cable mode disappears, but the sequence of global modes is preserved. The difference is the higher values of the frequencies of all modes due to the positive geometric stiffness of the cables. A good correlation is found with the frequencies reported in the literature [36]. The lowest six modal configurations of the Runyang suspension bridge are portrayed in Fig. 2. The aspect ratio of the reference geometry of the bridge as well as the scaling of the modal displacement components have been optimized for visualization purposes of the modal patterns.

For the *Hu Men* Suspension Bridge, the modal sequence for the stress-free bridge is the same as the Runyang bridge although the frequencies are higher due to the shorter span of the *Hu Men* (Table 2). For the prestressed condition, the only difference is that

the fourth mode is the second skew-symmetric vertical mode while the fifth mode is the lowest skew-symmetric lateral mode. The frequencies are all higher for this bridge.

Nonlinear precritical equilibrium paths The theoretical predictions based on the present nonlinear formulation have been first tested in the context of a static stability analysis since suspension bridges exhibit a substantial nonlinear precritical behavior due to the geometric nonlinearities of the cables. The aim of the analysis is to evaluate the nonlinear equilibrium paths of the bridge subject to vertical downward loads of increasing magnitude (quantified by the multiplier λ of the dead loads) and estimate the increase of stiffness suffered by the cables. On the other hand, path following analyses for increasing upward loads are performed to show the softening effect induced by the loss of tension in the cables. The geometric nonlinearities accounted for in the deck modeling are expected to give a marginal contribution to the increase of the overall stiffness of the bridge because of the assumed typical boundary conditions for the deck. The simply supported scheme does not allow the stretching effect to appear with the associated funicular-type load-bearing capacity so that the only nonlinear (geometric) contribution to the deck stiffness comes from nonlinear curvature effects.

Figures 3a and 3b show the nonlinear equilibrium paths obtained for the vertical displacement component of the deck and the maximum stretch of the cables compared with the paths obtained by linear theory. The

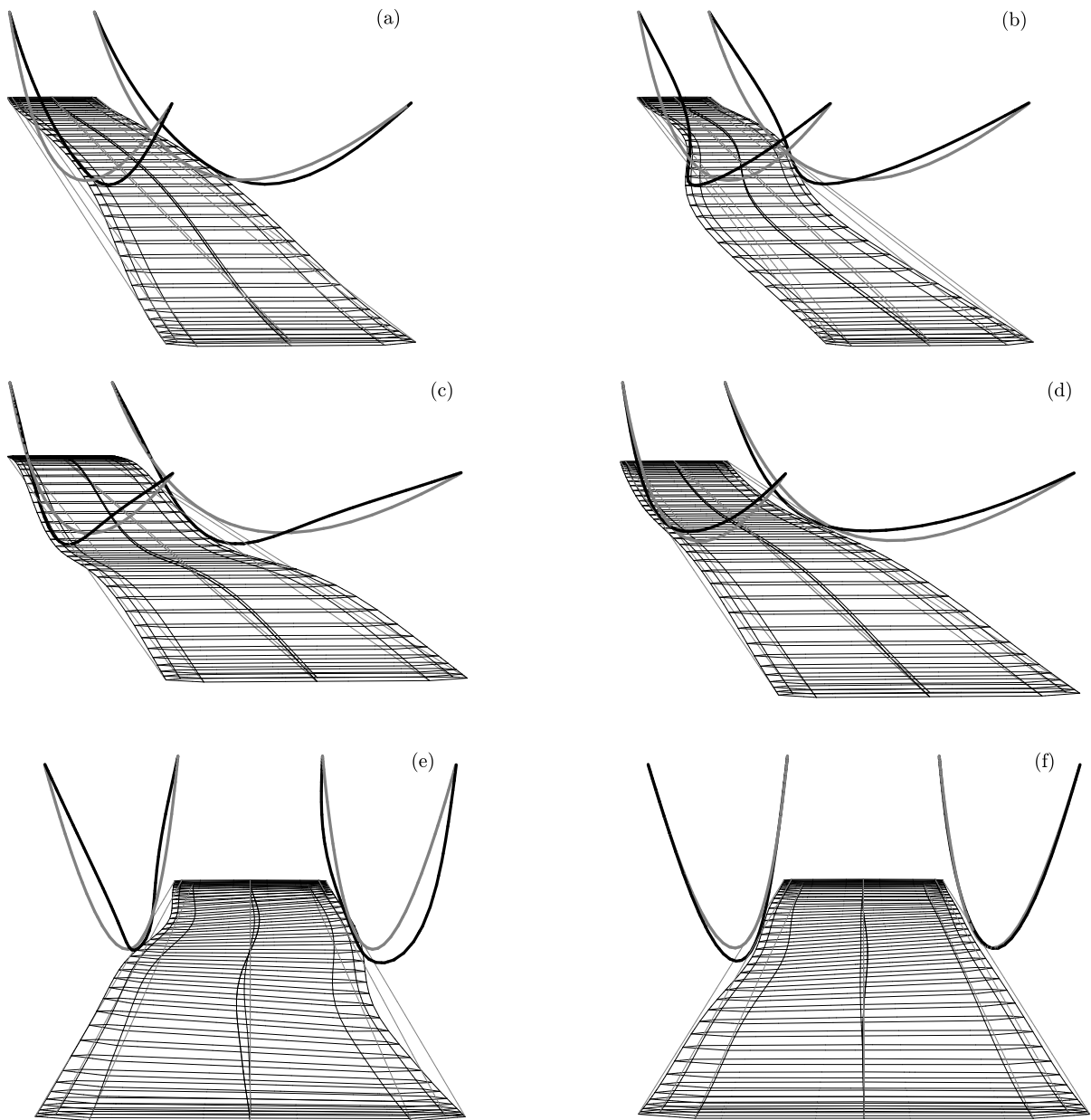


Fig. 2 The lowest six mode shapes of the *Runyang* suspension bridge

increment of stiffness due to the geometric nonlinearity is appreciable; the difference in the structural response becomes discernible already at low values of the dead load multiplier λ . Otherwise, very small increments of upward loads induce a pronounced softening behavior, which can be appreciated in Figs. 3c and 3d, due to the loss of tension suffered by the cables.

The equilibrium paths, shown in Figs. 4a and 4b, were obtained considering the bridge prestressed under the dead load f_2^o , subsequently subject to an incremental horizontal load f_1^o (Fig. 4a) and twisting couple c_3^o (Fig. 4b) proportional to the load f_2^o . These uniform loads are considered collinear with the directions of the aeroelastic forces so as to show that the geometric nonlinearities accounted for in the cables and

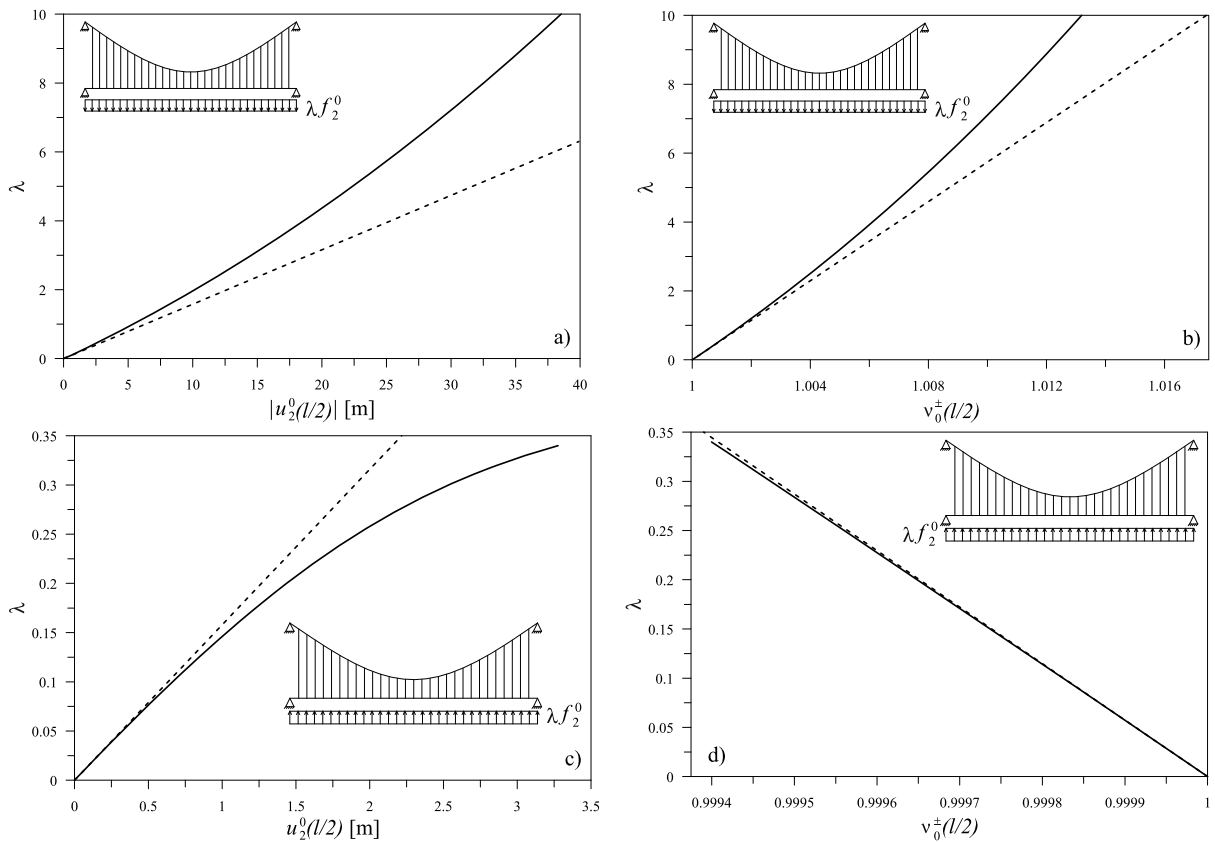


Fig. 3 Nonlinear equilibrium paths under vertical loads: (a) vertical (absolute) deck displacement and (b) cables stretch at the midspan for increasing load, (c) vertical deck displacement and (d) cables stretch at the midspan for decreasing load

deck-girder induce coupling between forces and displacements along different directions contrary to the predictions of linear theory. In fact, such effects vanish in the context of a linear model as suggested by the tangent lines to the curves at the origin of the plots in Figs. 4. Moreover, Figs. 5a and 5b show that the main consequence is the nontrivial, nonsymmetric stretch variations in the cables.

4 Aeroelastic instabilities

The main focus of the present work is the study of the aeroelastic response of suspension bridges in the context of the proposed nonlinear parametric model. Two kinds of stability analyses are carried out: torsional divergence and flutter. The first represents the bifurcation of the equilibrium state occurring when the bridge torsional stiffness becomes zero under the static part of the wind loads. This condition is studied

by calculating the whole nonlinear precritical equilibrium path under increasing aerostatic forces until the critical condition is signaled by the singularity of the stiffness matrix. Moreover, an eigenvalue analysis linearized about the configuration induced by the static aeroelastic load is performed, and the critical condition is identified when the first eigenvalue becomes purely real. On the other hand, flutter as a dynamic (Hopf) bifurcation is signaled by the crossing of a pair of eigenvalues on the imaginary axis, past which the perturbed equilibrium state gives rise to unbounded oscillations within a linear model. The flutter condition can be studied considering time-dependent simulations or the solution of a linear (or nonlinear) eigenvalue problem. The first approach allows to account for all nonlinearities, geometric and constitutive, and evaluate the flutter condition by analyzing the time histories of free vibration at different wind speeds, thus estimating the critical velocity when a limit cycle oscillation is reached.

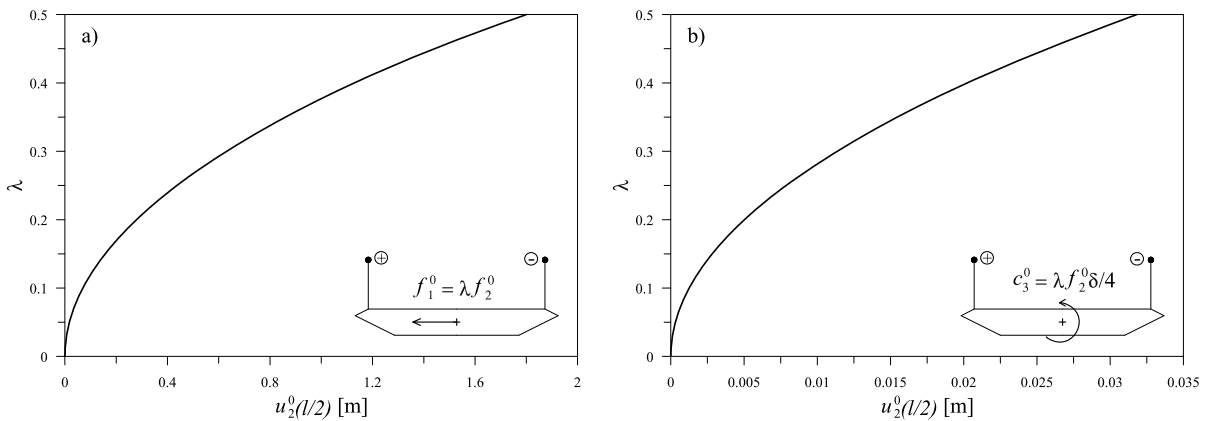


Fig. 4 Nonlinear equilibrium paths: vertical displacement of the midspan deck section for (a) increasing uniform horizontal load and (b) uniform torque

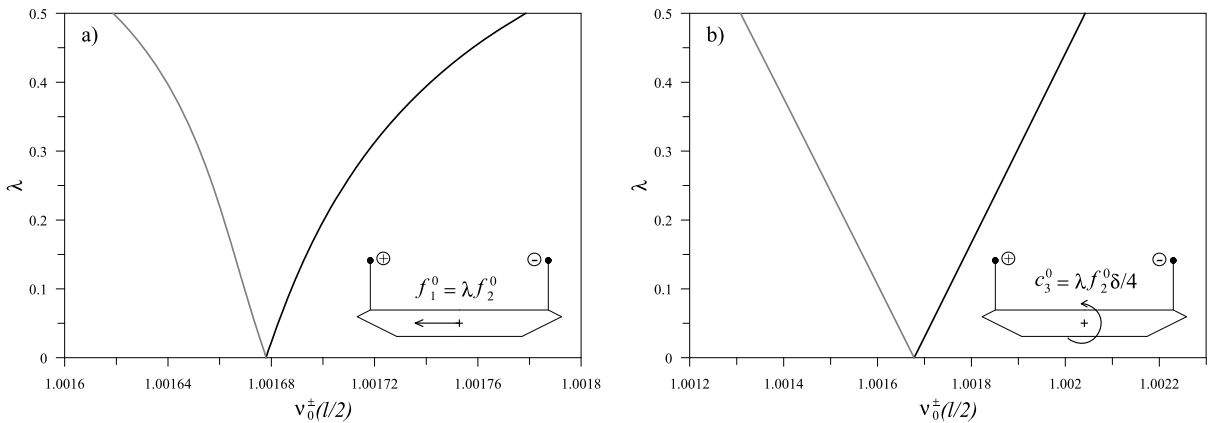


Fig. 5 Cables stretch at the midspan: (a) for increasing uniform horizontal load and (b) for increasing uniform torque. The gray lines refer to the cable “-”, the black lines refer to the cable “+”

The eigenvalue approach, pursued in this work, is based on the knowledge of the so-called *flutter derivatives*, experimentally obtained for each bridge section. The critical condition is obtained at the wind speed where the first complex-conjugate pair of eigenvalues crosses the imaginary axis. Figure 6 shows the aerodynamic (non-classical) convention assumed in this work: the lift force is assumed positive if upward, together with the vertical displacement, the drag force is oriented as the direction of the air flow and the moment is assumed positive if the section rotates in the counter-clockwise direction.

4.1 Torsional divergence

The aerostatic coefficients experimentally determined in wind tunnel tests for the sectional models of the

two considered bridges are shown in Fig. 7. The data obtained by digitalization of the original figures are used to determine by polynomial fitting the following expressions: for the Runyang bridge, $C_L^R(\alpha^E) = -0.0864 + 0.0744\alpha^E - 0.00195\alpha^{E2}$, $C_D^R(\alpha^E) = 0.7510 + 0.05867\alpha^E - 0.0066\alpha^{E2}$, $C_M^R(\alpha^E) = 0.0153 + 0.01654\alpha^E$; for the Hu Men bridge, the coefficients are: $C_L^{HM}(\alpha^E) = -0.024 + 0.0789\alpha^E$, $C_D^{HM}(\alpha^E) = 0.8276 + 0.0242535\alpha^E - 0.00815\alpha^{E2}$, $C_M^{HM}(\alpha^E) = 0.0153 + 0.0181\alpha^E$.

The interaction between the cables and the wind is accounted for by considering the drag force alone having the drag coefficient set to $C_D = 0.7$ as suggested in [50]. In the orthonormal frame $\{\bar{e}_1, \bar{e}_2, \bar{e}_3\}$, where \bar{e}_1 identifies the direction of the wind speed

Fig. 6 Positive aerodynamic forces

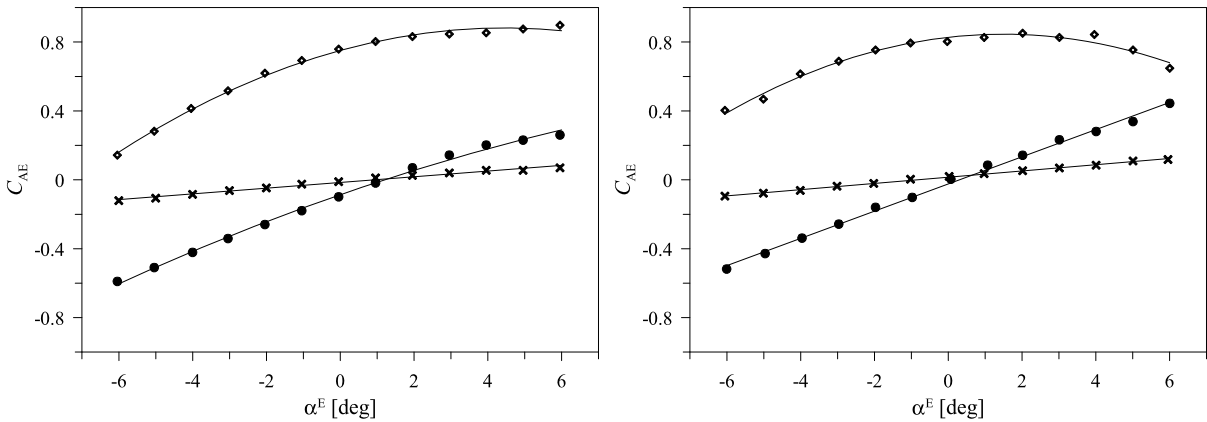
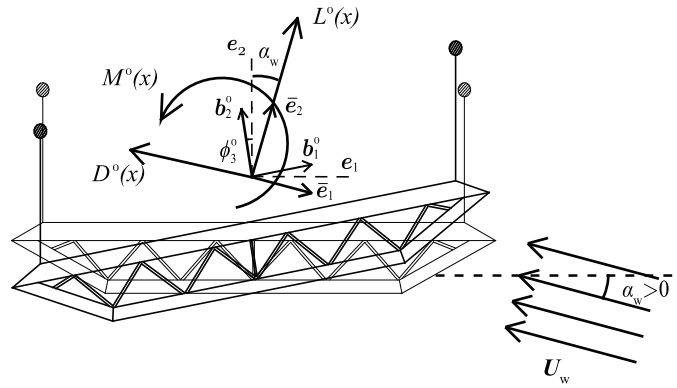


Fig. 7 Lift, drag and moment coefficients obtained in previous experiments and by polynomial fitting for (left) the Runyang bridge and (right) the Hu Men bridge

$U_w = -U_w \bar{e}_1$, \bar{e}_2 is the direction of the lift force and $\bar{e}_3 = \bar{e}_1 \times \bar{e}_2$, the nondimensional expressions of the forces per unit length of the deck generated by the static component U_w of the wind speed are expressed as

$$\begin{aligned}
 f_{AE}^o &= -D^o(x)\bar{e}_1 + L^o(x)\bar{e}_2, \\
 c_{AE}^o &= M^o(x)\bar{e}_3, \quad L^o(x) = \Gamma \delta C_L(\alpha^E), \\
 D^o(x) &= \Gamma \delta \bar{d} C_D(\alpha^E), \\
 M^o(x) &= \Gamma \delta^2 C_M(\alpha^E), \\
 f_{o,AE}^\pm &= -D_c^o(x)\bar{e}_1 = -0.7\Gamma \frac{d^c}{B} \bar{e}_1,
 \end{aligned}
 \tag{21}$$

where d^c is the cable diameter, $\alpha^E = \alpha_w + \phi_3^o$ is the effective angle of attack, B and D are the deck width

and height, respectively, (see Fig. 1) and

$$\Gamma = \frac{1}{2} \frac{\rho^a U_w^2}{\rho A^d \bar{\omega}^2}, \quad \delta = \frac{B}{l}, \quad \bar{d} = \frac{D}{B}. \tag{22}$$

The aerostatic forces (21) enter the equilibrium equations (11) through $f^o(x)$, $c^o(x)$ and $f_o^\pm(x)$.

A parametric nonlinear calculation is performed by increasing the aerostatic forces by a multiplier of the wind velocity U_w . The precritical equilibrium paths are evaluated for three initial wind angles of attack α_w . The evolution of all kinematic variables such as the vertical and horizontal deck displacements u_2^o and u_1^o and the twisting rotation ϕ_3^o can be observed in Figs. 8a and 8b referred to the Runyang suspension bridge. The dashed lines indicate the results of the linearized model while the solid lines describe the nonlinear predictions. For trivial or negative angles of attack, nonlinear analysis does not predict the appearance of torsional divergence since the lift forces are

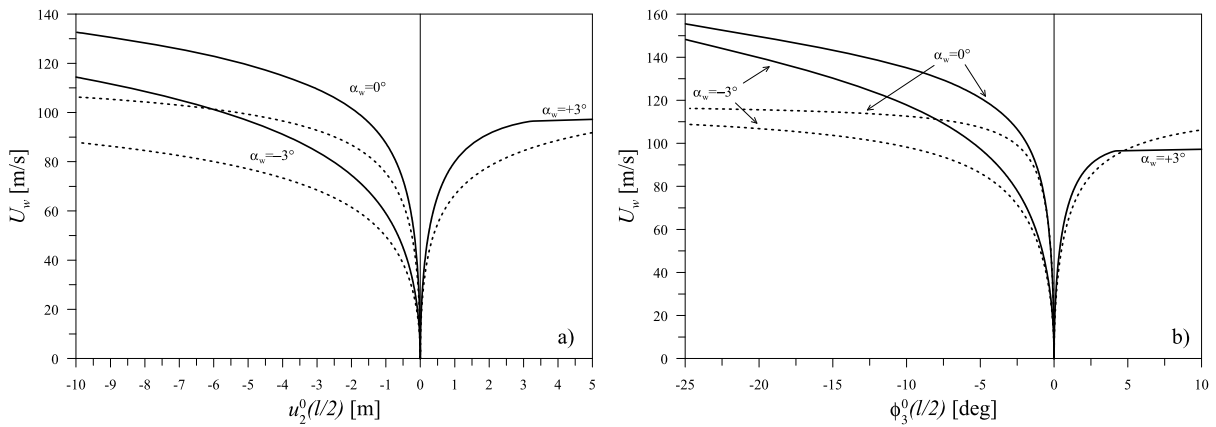


Fig. 8 Equilibrium paths of the Runyang bridge for increasing aeroelastic loads at different wind angles of attack α_w : **(a)** vertical displacement and **(b)** torsional rotation vs. wind velocity

U_w . The *dashed lines* refer to a linearized model, the *solid lines* refer to the proposed fully nonlinear model

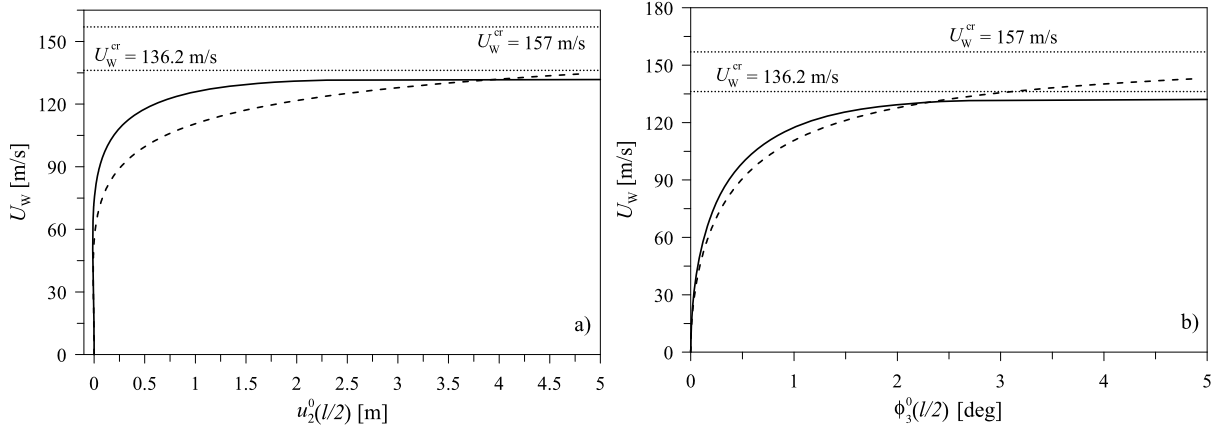


Fig. 9 Linear and nonlinear equilibrium paths of the Hu Men suspension bridge for increasing aeroelastic loads for $\alpha_w = 0^\circ$: **(a)** vertical displacement and **(b)** torsional rotation vs. wind velocity U_w

directed downward and act to increase the torsional stiffness of the bridge by inducing a tensioning of the suspension cables. On the contrary, linear analysis predicts torsional divergence erroneously since it neglects these nonlinear effects of the aerostatic forces on the bridge equilibrium. For $\alpha = +3^\circ$, nonlinear analysis predicts a critical speed at about 100 m/s while linear analysis yields a higher critical speed at about 112 m/s, as shown in Fig. 8b. The hierarchy of results predicted by linear vs. nonlinear analysis is not necessarily such that linear analysis is more conservative than nonlinear analysis as shown in this example. This is due to the fact that for positive angles the lift causes a loss

of tension in the cables entailing a torsional stiffness reduction, hence a lower critical speed.

The same analyses are conducted for the Hu Men suspension bridge for which a torsional divergence analysis is provided in [15]. Figure 9 shows the equilibrium paths obtained by the nonlinear model and compared with the typical path constructed by a linear model that neglects flexural-torsional coupling. A lower critical wind velocity is obtained by the proposed nonlinear model. The results are in good agreement with those of [15, 37]. It shows how the coupling of aerostatic forces leads to a decrease of the critical wind velocity.

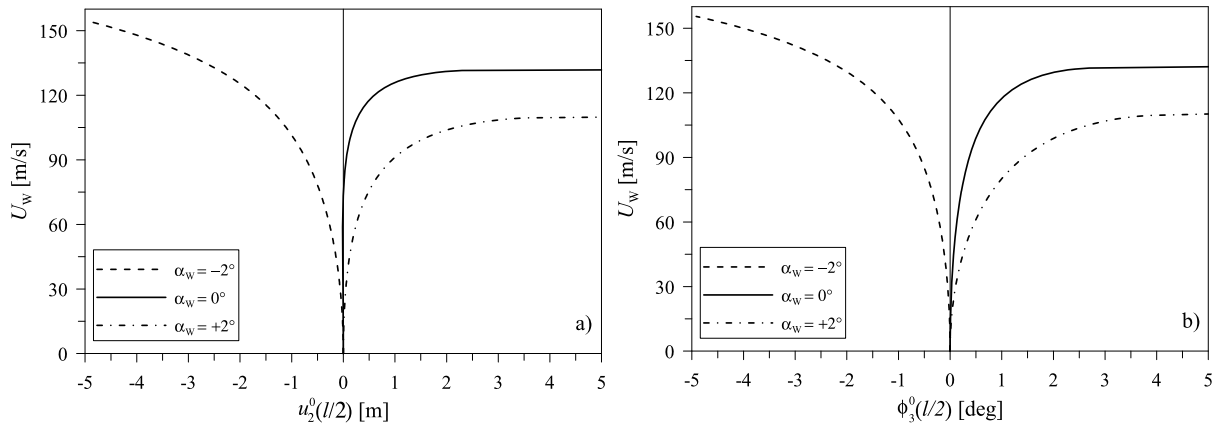


Fig. 10 Equilibrium paths of the Hu Men suspension bridge for increasing aeroelastic loads for different α_w : (a) vertical displacement and (b) torsional rotation vs. wind velocity U_w

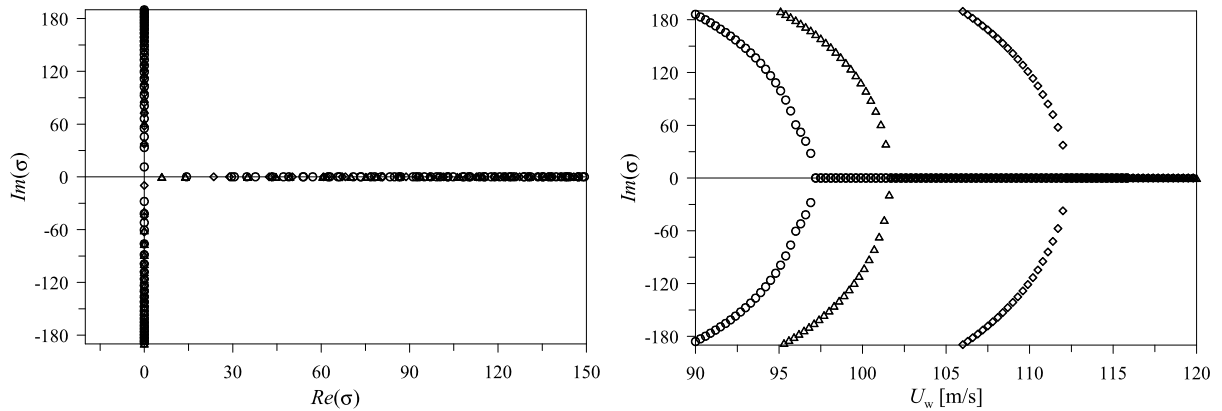


Fig. 11 The path of the lowest eigenvalue of the Runyang suspension bridge in the vicinity of the divergence bifurcation (left) and imaginary part vs. wind speed (right): circles stand for $\alpha_w = +3^\circ$, triangles stand for $\alpha_w = +2^\circ$, and diamonds stand for $\alpha_w = +1^\circ$

Figure 10 shows the nonlinear precritical paths for different initial wind angles of attack α_w .

The continuum formulation is also used for sensitivity analyses whose main results are shown in Figs. 14 and 15. Here, the geometric and constitutive characteristics of the Runyang and Hu Men Suspension Bridge, indicated respectively by subscripts “R” and “HM,” are taken as reference values about which some suitable variations are considered. The results indicate that due to finite rotations of the deck cross sections, the nondimensional torsional rigidity τ as well as the cables axial elastic stiffness κ^c have an important influence on the aeroelastic response. Less sensitivity of the critical speed is exhibited with respect to variations in the hangers stiffness ratio κ^h and the flexural bending ratio χ . In the same figures, the influ-

ence of the initial wind angle of attack of the wind on torsional divergence is shown.

The path traced by the eigenvalues as the wind speed is varied in the vicinity of the divergence bifurcation confirms the expected scenario according to which two complex conjugate eigenvalues move on the imaginary axis toward the origin and coalesce into it at the bifurcation as shown in Fig. 11 (left) referred to the Runyang bridge. On the other hand, the sensitivity of the frequency of the mode that undergoes divergence (imaginary part of the eigenvalue) with respect to the wind speed can be appreciated in Fig. 11 (right) where the three angles of attack $\alpha_w = (+3^\circ, +2^\circ, +1^\circ)$ are considered. Similar behaviors are observed in the vicinity of the divergence bifurcation of the Hu Men suspension bridge in Figs. 12.

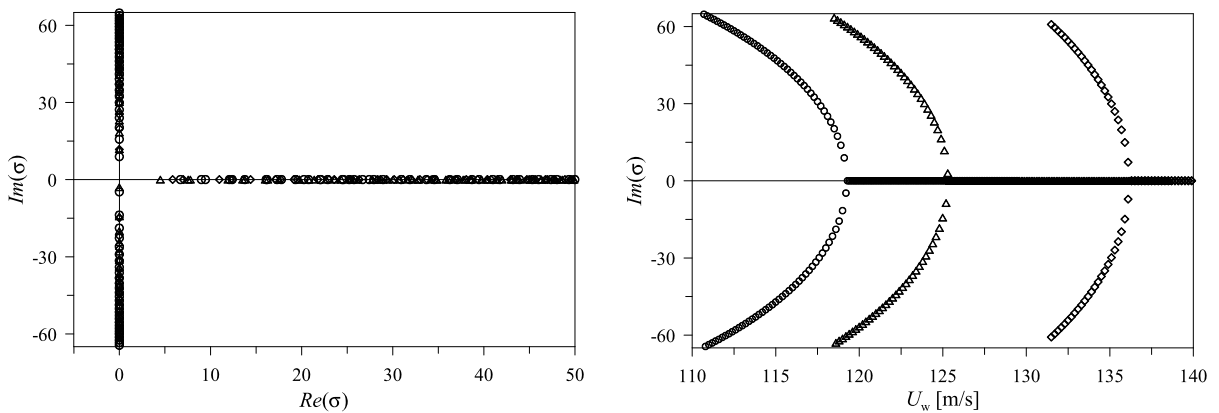
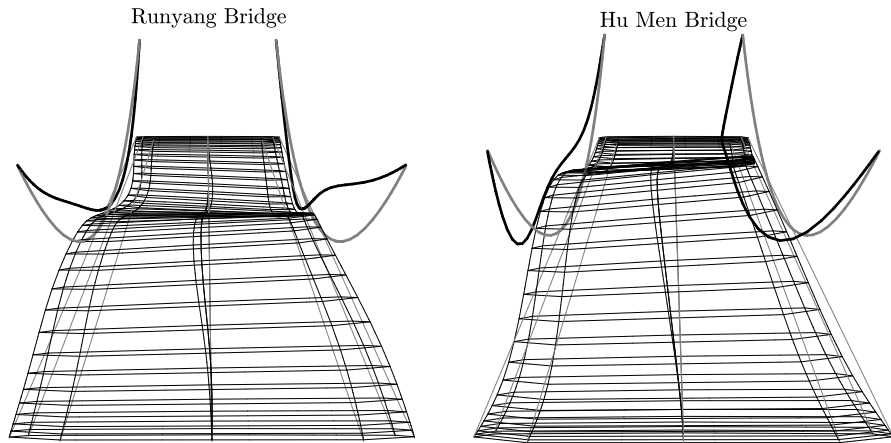


Fig. 12 The paths of the lowest eigenvalue of the Hu Men suspension bridge in the vicinity of the divergence bifurcation: *circles* stand for $\alpha_w = +2^\circ$, *triangles* stand for $\alpha_w = +1^\circ$, and *diamonds* stand for $\alpha_w = 0^\circ$

Fig. 13 Mode undergoing divergence for the Runyang suspension bridge (*left*) when $\alpha_w = +1^\circ$ and $U_w^{cr} = 111.2$ m/s and for the Hu Men suspension bridge (*right*) when $\alpha_w = 0^\circ$ and $U_w^{cr} = 136.2$ m/s



The flexural/torsional modes that undergo divergence for the Runyang and Hu Men bridges in the critical state are shown in Fig. 13.

4.2 Flutter

The critical wind speeds at the onset of torsional divergence are usually higher than the flutter speeds. To compute the onset of flutter, the classical complex eigenvalue problem is tackled employing the representation of the aerodynamic forces by the use of flutter derivatives. Two approaches are implemented. The first approach proposed by [24] consists of defining a complex nonlinear eigenvalue problem and solving it by increasing the wind speed U_w about the aerostatic equilibrium until the condition of be purely imaginary eigenvalues is found. On the other hand, several linear eigenvalue problems can be solved for each value

of U_w to obtain the actual eigenvalues in the vicinity of the flutter condition. The first approach can be easily used for a two-dof sectional model, as in [25], although it is a nonclassical procedure for multi-dof systems. The results obtained by the two approaches are discussed in the following.

The expressions of the aerodynamic forces per unit reference length, in terms of the experimental aeroelastic derivatives H_i^*, A_i^* , $i = 1, \dots, 4$, are given in (23). The latter are then introduced in the equations of motion (12) through $\check{f}(x, t)$ and $\check{c}(x, t)$ as follows:

$$\check{f}_{AE} = f_{AE}^0 + L(x, t)\bar{e}_2,$$

$$\check{c}_{AE} = c_{AE}^0 + M(x, t)\bar{e}_3,$$

$$L(x, t) = \frac{1}{2}\rho^a B U_w^2 \left(\frac{K}{U_w} H_1^* \partial_t u_2 + \frac{K B}{U_w} H_2^* \partial_t \phi_3 \right)$$

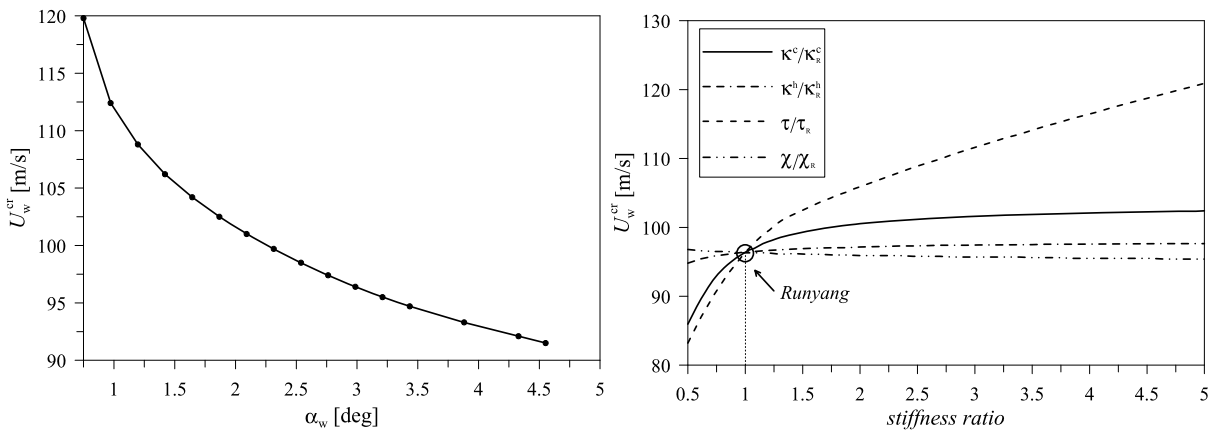


Fig. 14 Sensitivity analyses for α_w and the stiffness parameters ratios vs. the critical wind speed. Subscript “R” refers to the Runyang bridge parameters

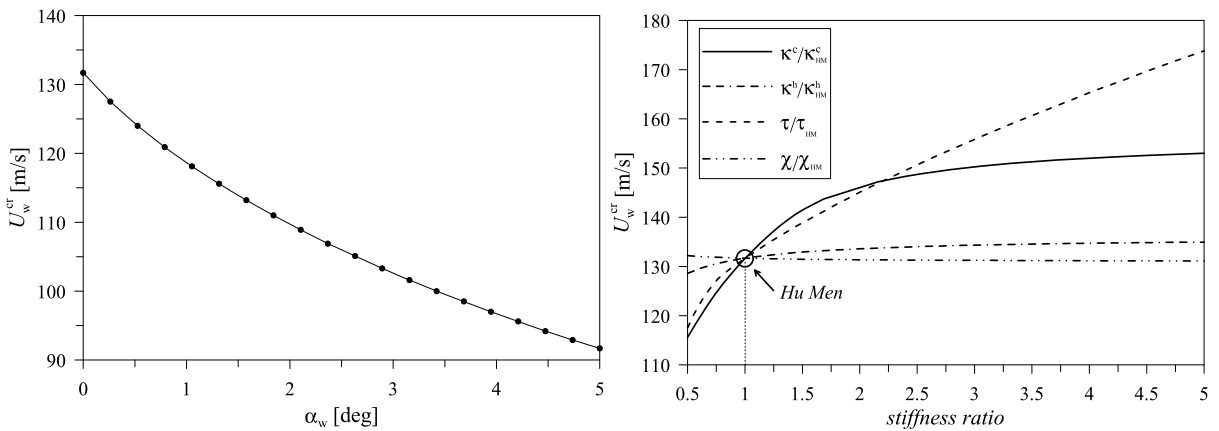


Fig. 15 Sensitivity analyses for α_w and the stiffness parameters ratios vs. the critical wind speed. Subscript “HM” refers to the Hu Men bridge parameters

$$\begin{aligned}
 &+ K^2 H_3^* \phi_3 + \frac{K^2}{B} H_4^* u_2), \tag{23} \\
 M(x, t) = &\frac{1}{2} \rho^a B^2 U_w^2 \left(\frac{K}{U_w} A_1^* \partial_t u_2 + \frac{KB}{U_w} A_2^* \partial_t \phi_3 \right. \\
 &\left. + K^2 A_3^* \phi_3 + \frac{K^2}{B} A_4^* u_2 \right).
 \end{aligned}$$

In consonance with classical notations, ρ^a denotes the air density, B is the deck depth, U_w is the dimensional wind velocity, and K is the reduced frequency defined as $K := \omega B / U_w$, where ω is the circular oscillation frequency of the mode involved in flutter. In Figs. 16 and 17, the experimental values of the flutter derivatives calculated for the deck cross section of the Runyang suspension bridge, proposed in [14], are given together with the classical derivatives calculated for a

rectangular (streamlined) section of ratio $B/D \approx 14.3$ reported in [22]. Data are calculated for increasing values of the reduced velocity $U_r = 2\pi/K$.

Complex eigenvalue problem The expressions of the aerodynamic forces are first cast in a suitable nondimensional form. By introducing the parameters $\Gamma_f = 12\rho^a B l / \rho A^d$ and $\delta = B/l$, the nondimensional form of Eq. (23) becomes

$$\begin{aligned}
 L(x, t) = &\Gamma_f \delta \left[\sigma H_1^* \partial_t u_2(x, t) + \sigma \delta H_2^* \partial_t \phi_3(x, t) \right. \\
 &\left. + \sigma^2 \delta H_3^* \phi_3(x, t) + \sigma^2 H_4^* u_2(x, t) \right], \\
 M(x, t) = &\Gamma_f \delta^2 \left[\sigma A_1^* \partial_t u_2(x, t) + \sigma \delta A_2^* \partial_t \phi_3(x, t) \right. \\
 &\left. + \sigma^2 \delta A_3^* \phi_3(x, t) + \sigma^2 A_4^* u_2(x, t) \right], \tag{24}
 \end{aligned}$$

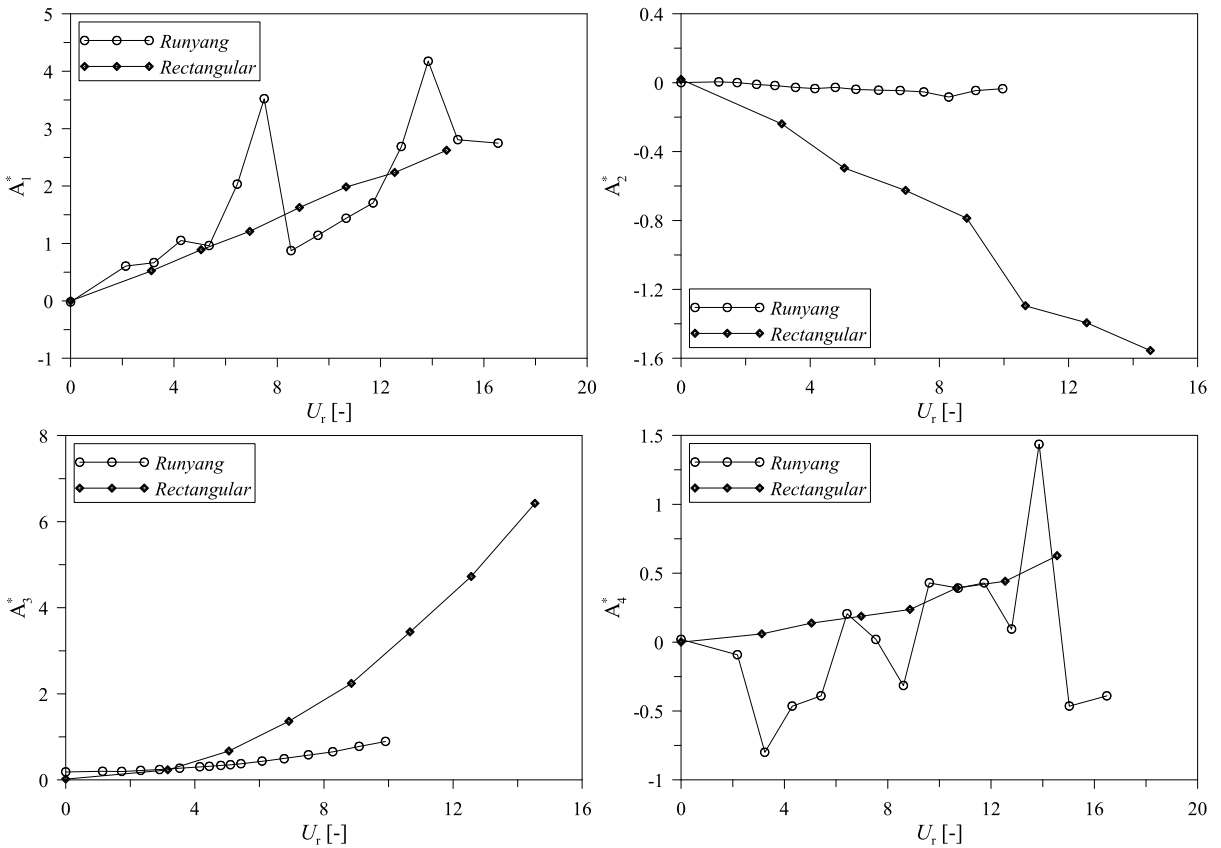


Fig. 16 Aeroelastic derivatives A_i^* for $\alpha_w = 0^\circ$: Runyang deck cross-section and rectangular section

where σ is the nondimensional circular frequency $\sigma = \omega/\bar{\omega}$. By assuming the solution of the dynamic problem in the form $[\mathbf{u}(x, t), \phi_j(x, t), \mathbf{v}^\pm(x, t)] = [\bar{\mathbf{u}}(x), \bar{\phi}_j(x), \bar{\mathbf{v}}^\pm(x)]e^{i\sigma t}$, $j = 1, 2, 3$, the flutter condition is found when a pair of eigenvalues $\sigma = \sigma_R + i\sigma_I$ becomes purely real. In terms of the eigenvalue σ , the aerodynamic nondimensional loads can be written as

$$\begin{aligned} \bar{L}(x, t) &= \Gamma_f \delta \sigma^2 (i H_1^* \bar{u}_2 + i \delta H_2^* \bar{\phi}_3 \\ &\quad + \delta H_3^* \bar{\phi}_3 + H_4^* \bar{u}_2) e^{i\sigma t}, \\ \bar{M}(x, t) &= \Gamma_f \delta^2 \sigma^2 (i A_1^* \bar{u}_2 + i \delta A_2^* \bar{\phi}_3 \\ &\quad + \delta A_3^* \bar{\phi}_3 + A_4^* \bar{u}_2) e^{i\sigma t}. \end{aligned}$$

Accordingly, the nondimensional inertia and damping forces, by neglecting the contributions of the rotatory inertia and damping about axes $\bar{\mathbf{b}}_1$ and $\bar{\mathbf{b}}_2$, can be ex-

pressed as

$$\begin{aligned} \bar{\mathbf{f}}_M^\pm + \bar{\mathbf{f}}_D^\pm &= [-\sigma^2 \varrho^c \sec \theta_0^\pm(x) \bar{\mathbf{v}}^\pm(x) \\ &\quad + i \sigma D_j^c \bar{\mathbf{v}}^\pm(x)] e^{i\sigma t}, \\ \bar{\mathbf{f}}_M + \bar{\mathbf{f}}_D &= [-\sigma^2 \bar{\mathbf{u}}(x) + i \sigma D_j^d \bar{\mathbf{u}}(x)] e^{i\sigma t}, \quad (25) \\ \bar{\mathbf{c}}_M + \bar{\mathbf{c}}_D &= [-\sigma^2 J^m \bar{\phi}_3(x) \\ &\quad + i \sigma D_j^T \bar{\phi}_3(x)] e^{i\sigma t} \mathbf{b}_3. \end{aligned}$$

Classical eigenvalue problem The solution of the dynamic problem is here assumed in the form $[\mathbf{u}(x, t), \phi_j(x, t), \mathbf{v}^\pm(x, t)] = [\bar{\mathbf{u}}(x), \bar{\phi}_j(x), \bar{\mathbf{v}}^\pm(x)]e^{i\sigma t}$, $j = 1, 2, 3$. Accordingly, the flutter condition is obtained when a pair of eigenvalues $\sigma = \sigma_R + i\sigma_I$ becomes purely imaginary. By introducing the parameter $\bar{U} := U_w/(\bar{\omega}l)$, the aerodynamic nondimensional loads can

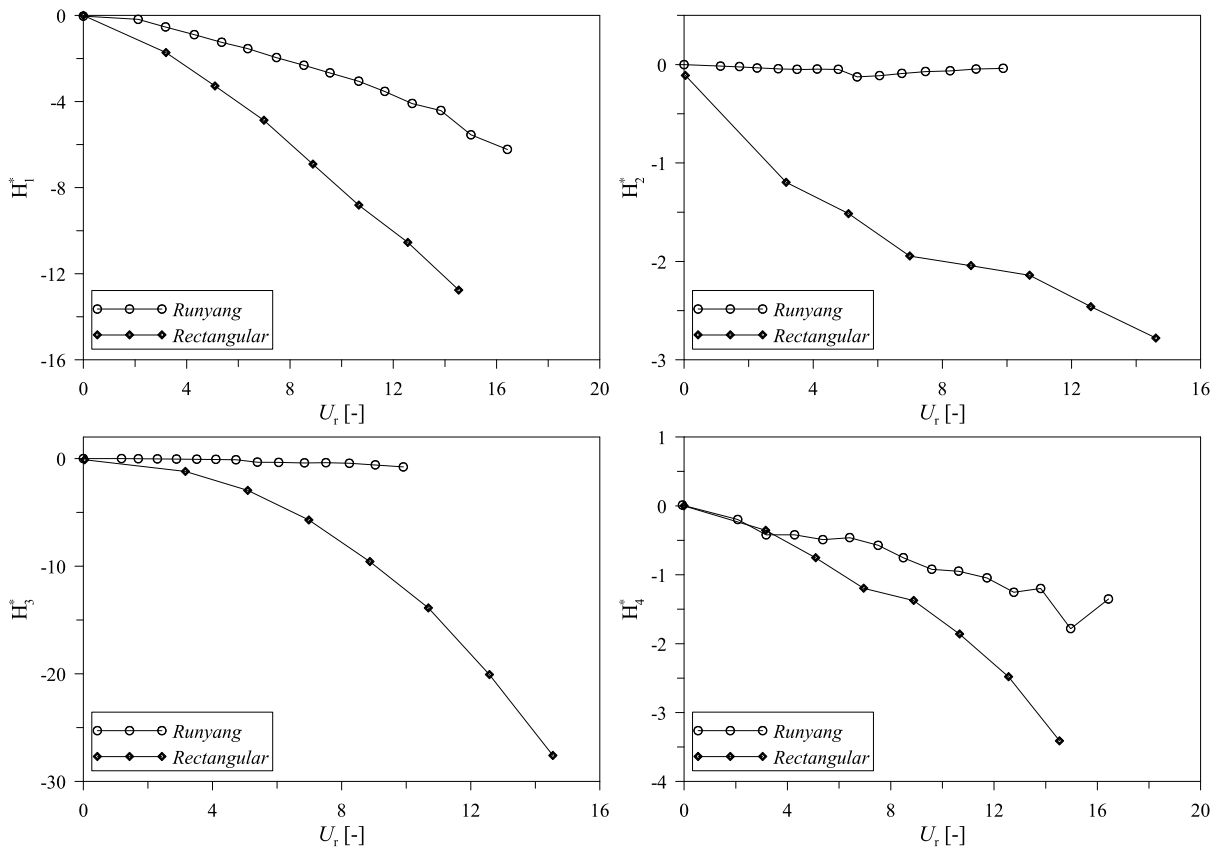


Fig. 17 Aeroelastic derivatives \$H_i^*\$ for \$\alpha_w = 0^\circ\$: Runyang deck cross-section and rectangular section

be written in terms of the eigenvalue \$\sigma\$ as

$$\begin{aligned}
 \bar{L}(x, t) &= \Gamma_f \bar{U}^2 \left(\frac{K H_1^*}{\bar{U}} \sigma \bar{u}_2 + \delta \frac{K H_2^*}{\bar{U}} \sigma \bar{\phi}_3 \right. \\
 &\quad \left. + K^2 H_3^* \bar{\phi}_3 + \frac{K^2 H_4^*}{\delta} \bar{u}_2 \right) e^{\sigma t}, \\
 \bar{M}(x, t) &= \Gamma_f \delta \bar{U}^2 \left(\frac{K A_1^*}{\bar{U}} \sigma \bar{u}_2 + \delta \frac{K A_2^*}{\bar{U}} \sigma \bar{\phi}_3 \right. \\
 &\quad \left. + K^2 A_3^* \bar{\phi}_3 + \frac{K^2 A_4^*}{\delta} \bar{u}_2 \right) e^{\sigma t}.
 \end{aligned} \tag{26}$$

On the other hand, the nondimensional inertia and damping forces can be written as

$$\begin{aligned}
 \bar{f}_M^\pm + \bar{f}_D^\pm &= [\sigma^2 \varrho^c \sec \theta_\sigma^\pm(x) \bar{v}^\pm(x) \\
 &\quad + \sigma D_j^c \bar{v}^\pm(x)] e^{\sigma t}, \\
 \bar{f}_M + \bar{f}_D &= [\sigma^2 \bar{u}(x) + \sigma D_j^d \bar{u}(x)] e^{\sigma t}, \\
 \bar{c}_M + \bar{c}_D &= [\sigma^2 J^m \bar{\phi}_3(x) + \sigma D_j^T \bar{\phi}_3(x)] e^{\sigma t} \mathbf{b}_3.
 \end{aligned} \tag{27}$$

Figure 18 shows variation of the logarithmic decrement \$\Delta\$ and frequency \$f\$ of the torsional and flexural modes with the wind speed \$U_w\$. On other hand, the Fig. 19 shows the flutter mode shape. The results obtained by the two eigenvalue problems are compared. The dashed lines indicate the Scanlan procedure, the solid lines represent the iterative procedure. The black lines refer to the symmetric modes while the gray lines describe the skew-symmetric modes. The flutter condition is attained for the symmetric torsional mode where the logarithmic decrement vanishes (see Fig. 18a). On the other hand, the skew-symmetric torsional mode and the lowest two bending modes are always positively damped. The Scanlan procedure and the iterative procedure differ slightly in terms of predicted frequency of the torsional mode while they do differ in terms of logarithmic decrements for all modes and the frequency of the bending modes. In Fig. 20, the same flutter analysis for the Runyang bridge is conducted using the smoother flutter derivatives referred

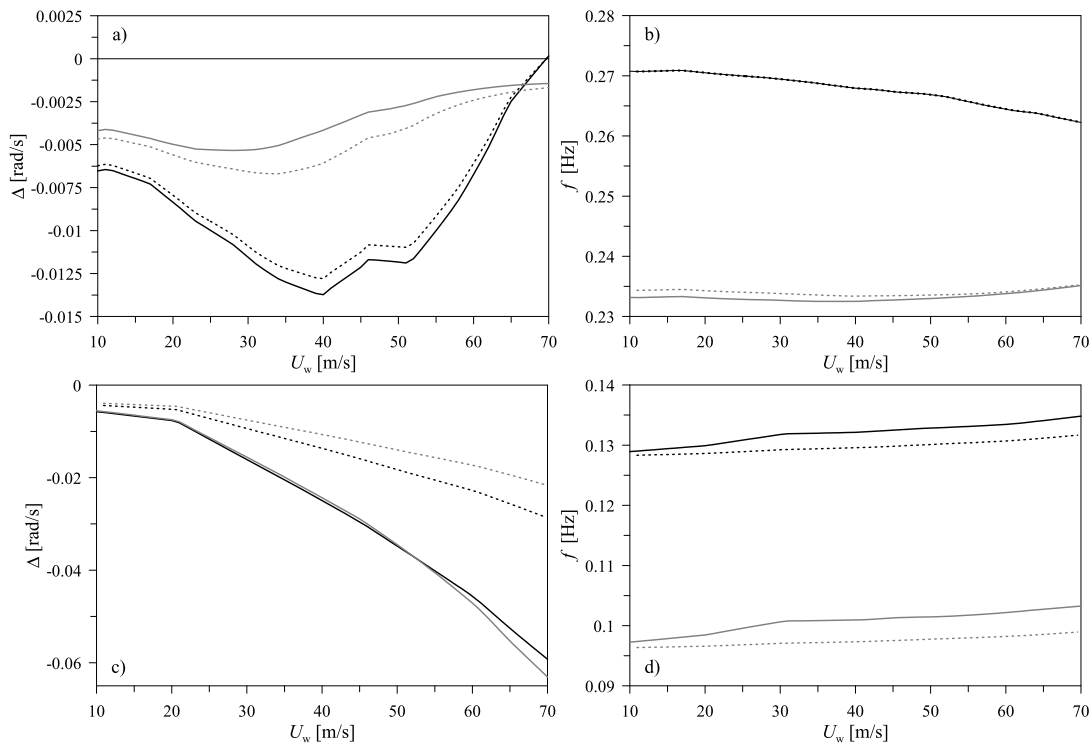


Fig. 18 Flutter investigation for the Runyang bridge using the experimental aerodynamic derivatives for $\alpha_w = 0^\circ$: (a) and (b) torsional modes, (c) and (d) vertical bending modes. The dashed

lines indicate the Scanlan procedure, the solid lines represent the iterative procedure. The black lines refer to the symmetric modes; the gray lines refer to the skew-symmetric modes

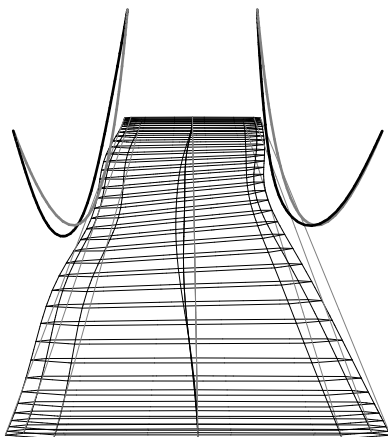


Fig. 19 Flutter mode shape of the Runyang suspension bridge for $\alpha_w = 0^\circ$

to the rectangular cross section. The main difference is that the mode that undergoes flutter is the lowest skew-symmetric torsional mode instead of the symmetric mode. The comparison between the Scanlan

procedure and the iterative procedure shows the same kind of trends outlined in the previous case. Figure 21 shows the expected high sensitivity of the flutter speed with respect to the damping ratio and the multiplier of the dead loads. For example, increasing the damping ratio from 0.03 % to 0.5 %, the flutter speed goes from 60 to 70 m/s. Moreover, amplifying the dead loads by 50 % makes the flutter speed increase from 70 to 78 m/s, a known trend for suspension bridges that has led to counteract flutter under high winds by aligning heavy trucks on the lanes of some bridges in a few exceptional cases.

These studies are possible only in the context of a fully nonlinear problem formulation.

5 Summary and conclusions

A geometrically exact parametric model of suspension bridges was formulated and the nonlinear equations of motion were obtained via a Lagrangian formulation. The nonlinear system of partial differential equations

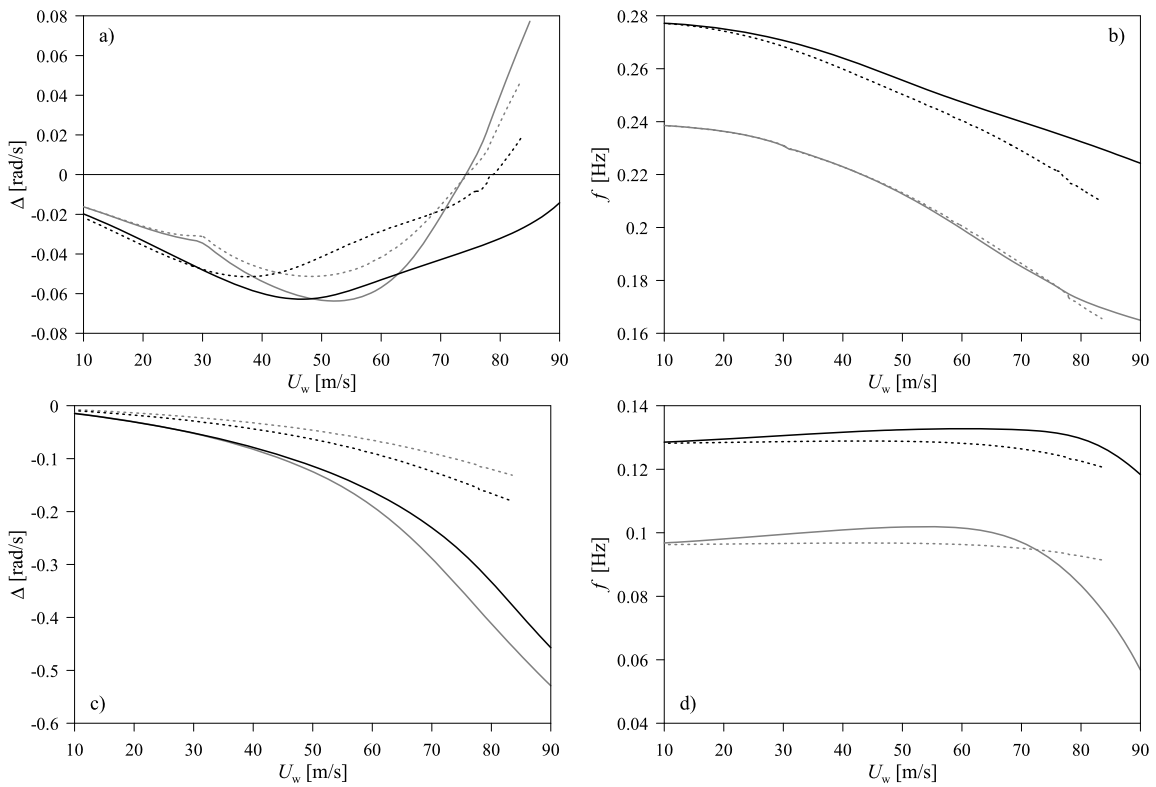


Fig. 20 Flutter investigation for the Runyang bridge using the aeroelastic derivatives of a rectangular cross section: (a) and (b) torsional modes, (c) and (d) vertical bending modes. The dashed

lines indicate the Scanlan procedure, the solid lines represent the iterative procedure. The black lines refer to the symmetric modes; the gray lines refer to the skew-symmetric modes

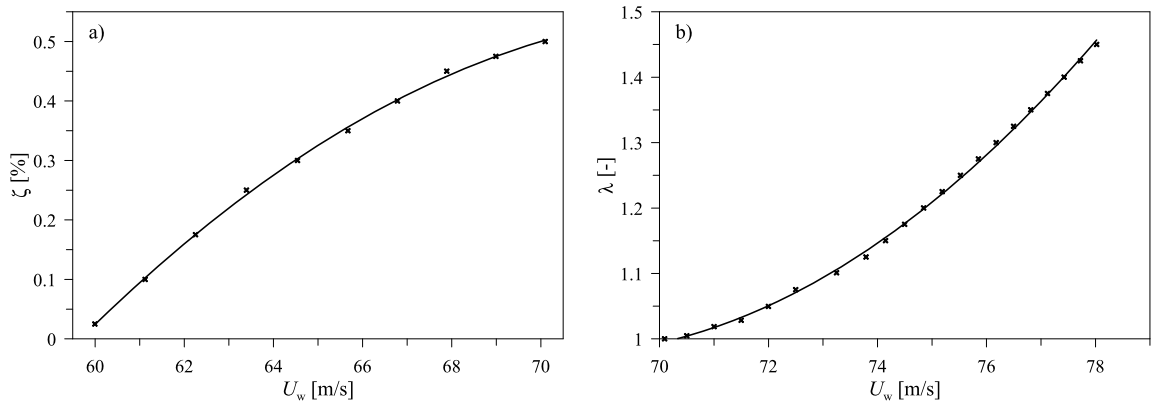


Fig. 21 Sensitivity of the flutter speed to: (a) the structural damping ratio ζ , (b) the dead load multiplier λ for $\alpha_w = 0^\circ$

governing the equilibrium and dynamic aeroelastic response of suspension bridges was solved via a FE discretization considering the structural and aerodynamic characteristics of two case-study bridges, the Runyang and the Hu Men suspension bridges.

A preliminary modal analysis was carried out to compare the natural frequencies evaluated by the proposed model with literature results. A good agreement was found for both case studies. Parametric analyses were performed to highlight the influence of the ca-

bles geometric stiffness in the nonlinear equilibrium and dynamic response of the bridge. The characteristic mechanical asymmetry is exhibited as a softening or a hardening behavior depending on whether the loads are upward or downward. This is due to a loss of tension or to an increase of tension in the suspension cables. This nonlinear mechanical feature due to the suspension cables turns out to affect profoundly the aeroelastic limit states.

Static and dynamic bifurcation analyses were carried out to investigate the occurrence of torsional divergence and flutter. The eigenvalue problem, obtained by linearization about the prestressed configuration induced by dead and aeroelastic loads, was solved. The determined bifurcation diagrams showed the high sensitivity of the bridge flexural-torsional frequency close to the critical condition. These studies conducted for both bridges have proved the sensitivity of the critical condition with respect to the stiffness bridge properties (namely, the elastic torsional and bending stiffness, the elastogeometric stiffness of the suspension cables) and the initial wind angle of attack.

The flutter phenomenon is studied in the frequency domain by two eigenvalue approaches, namely, the approach suggested by Scanlan and the classic (iterative) modal analysis approach. The latter gives the actual dependence of the eigenvalues from the aeroelastic forces near flutter. The differences for the frequencies and modal damping ratios calculated by this method and the Scanlan procedure tend to vanish in the vicinity of the critical condition where the coalesce. The onset of flutter is very sensitive to the initial wind angle of attack, the damping ratio, and the bridge prestress condition caused by dead loads.

Acknowledgements This material is based on work supported by the Ministry of Education, University, and Scientific Research under a PRIN Grant awarded to WL. The authors also gratefully acknowledge The National Science Foundation (grant NSF-CMMI-1031036) for providing further partial support.

Appendix

The nine components of the rotation matrix \mathbf{R}^o are given by

$$\begin{aligned}
 R_{11}^o &= \cos \phi_2^o \cos \phi_3^o, \\
 R_{12}^o &= -\cos \phi_2^o \sin \phi_3^o, \\
 R_{13}^o &= \sin \phi_2^o, \\
 R_{21}^o &= \sin \phi_1^o \sin \phi_2^o \cos \phi_3^o + \cos \phi_1^o \sin \phi_3^o, \\
 R_{22}^o &= \cos \phi_1^o \cos \phi_3^o - \sin \phi_1^o \sin \phi_2^o \sin \phi_3^o, \\
 R_{23}^o &= -\sin \phi_1^o \cos \phi_2^o, \\
 R_{31}^o &= \sin \phi_1^o \sin \phi_3^o - \cos \phi_1^o \sin \phi_2^o \cos \phi_3^o, \\
 R_{32}^o &= \cos \phi_1^o \sin \phi_2^o \sin \phi_3^o + \sin \phi_1^o \cos \phi_3^o, \\
 R_{33}^o &= \cos \phi_1^o \cos \phi_2^o.
 \end{aligned}
 \tag{28}$$

The vectors representing the rotations of the deck cross-section projected into the global frame $\{\mathbf{e}_1, \mathbf{e}_2, \mathbf{e}_3\}$ can be defined as:

$$\begin{aligned}
 \Psi^o &= [\psi_1^o \ \psi_2^o \ \psi_3^o]^T, \quad \check{\Psi} = [\check{\psi}_1, \check{\psi}_2, \check{\psi}_3]^T, \\
 \psi_1^o &= \phi_1^o + \phi_3^o \sin \phi_2^o, \\
 \psi_2^o &= \phi_2^o \cos \phi_1^o - \phi_3^o \sin \phi_1^o \cos \phi_2^o, \\
 \psi_3^o &= \phi_2^o \sin \phi_1^o + \phi_3^o \cos \phi_1^o \cos \phi_2^o, \\
 \check{\psi}_1 &= \phi_1 \cos \phi_2^o \cos \phi_3^o + \phi_2 (\sin \phi_2^o \sin \phi_1 \\
 &\quad - \cos \phi_2^o \sin \phi_3^o \cos \phi_1) \\
 &\quad + \phi_3 (\sin \phi_2^o \cos \phi_1 \cos \phi_2 \\
 &\quad + \cos \phi_2^o \sin \phi_3^o \sin \phi_1 \cos \phi_2 \\
 &\quad + \cos \phi_2^o \cos \phi_3^o \sin \phi_2), \\
 \check{\psi}_2 &= \phi_1 (\sin \phi_1^o \sin \phi_2^o \cos \phi_3^o + \cos \phi_1^o \sin \phi_3^o) \\
 &\quad + \phi_2 [\cos \phi_1 (\cos \phi_1^o \cos \phi_3^o \\
 &\quad - \sin \phi_1^o \sin \phi_2^o \sin \phi_3^o) - \sin \phi_1^o \cos \phi_2^o \sin \phi_1] \\
 &\quad + \phi_3 [-\sin \phi_1^o \cos \phi_2^o \cos \phi_1 \cos \phi_2 \\
 &\quad - \sin \phi_1 \cos \phi_2 (\cos \phi_1^o \cos \phi_3^o \\
 &\quad - \sin \phi_1^o \sin \phi_2^o \sin \phi_3^o) \\
 &\quad + \sin \phi_2 (\sin \phi_1^o \sin \phi_2^o \cos \phi_3^o + \cos \phi_1^o \sin \phi_3^o)], \\
 \check{\psi}_3 &= \phi_1 (\sin \phi_1^o \sin \phi_3^o - \cos \phi_1^o \sin \phi_2^o \cos \phi_3^o) \\
 &\quad + \phi_2 [\cos \phi_1 (\sin \phi_1^o \cos \phi_3^o \\
 &\quad + \cos \phi_1^o \sin \phi_2^o \sin \phi_3^o) + \cos \phi_1^o \cos \phi_2^o \sin \phi_1] \\
 &\quad + \phi_3 [\cos \phi_1^o \cos \phi_2^o \cos \phi_1 \cos \phi_2 \\
 &\quad - \sin \phi_1 \cos \phi_2 (\sin \phi_1^o \cos \phi_3^o \\
 &\quad + \cos \phi_1^o \sin \phi_2^o \sin \phi_3^o) + \sin \phi_2 (\sin \phi_1^o \sin \phi_3^o \\
 &\quad - \cos \phi_1^o \sin \phi_2^o \cos \phi_3^o)].
 \end{aligned}
 \tag{29}$$

(30)

References

1. Irvine, H.M.: Cablestructures. MIT Press, Cambridge (1981)
2. Abdel-Ghaffar, A.M.: Free lateral vibrations of suspension bridges. *J. Struct. Div.* **104**(3), 503–525 (1978)
3. Abdel-Ghaffar, A.M.: Free torsional vibrations of suspension bridges. *J. Struct. Div.* **105**(4), 767–788 (1979)
4. Abdel-Ghaffar, A.M.: Vertical vibration analysis of suspension bridges. *J. Struct. Div.* **106**(10), 2053–2075 (1980)
5. Abdel-Ghaffar, A.M.: Suspension bridge vibration: continuum formulation. *J. Eng. Mech. Div.* **108**(6), 1215–1232 (1982)
6. Abdel-Ghaffar, A.M., Rubin, L.I.: Nonlinear free vibrations of suspension bridges: theory. *J. Eng. Mech.* **109**, 313–329 (1983)
7. Abdel-Ghaffar, A.M., Rubin, L.I.: Nonlinear free vibrations of suspension bridges: application. *J. Eng. Mech.* **109**, 330–345 (1983)
8. Abdel-Rohman, M., Nayfeh, A.H.: Passive control of nonlinear oscillations in bridges. *J. Eng. Mech.* **113**, 1694–1708 (1987)
9. Abdel-Rohman, M., Nayfeh, A.H.: Active control of nonlinear oscillations in bridges. *J. Eng. Mech.* **113**, 335–349 (1987)
10. Çevika, M., Pakdemirlib, M.: Non-linear vibrations of suspension bridges with external excitation. *Int. J. Non-Linear Mech.* **40**, 901–923 (2005)
11. Malík, J.: Nonlinear models of suspension bridges. *J. Math. Anal. Appl.* **321**, 828–850 (2006)
12. Malík, J.: Generalized nonlinear models of suspension bridges. *J. Math. Anal. Appl.* **324**, 1288–1296 (2006)
13. Boonyapinyo, V., Yamada, H., Miyata, T.: Wind-induced nonlinear lateral-torsional buckling of cable-stayed bridges. *J. Struct. Eng.* **120**(2), 486–506 (1994)
14. Zhang, X., Xiang, H., Sun, B.: Nonlinear aerostatic and aerodynamic analysis of long-span suspension bridges considering wind-structure interactions. *J. Wind Eng. Ind. Aerodyn.* **92**, 431–439 (2002)
15. Cheng, J., Jiang, J., Xiao, R.: Aerostatic stability analysis of suspension bridges under parametric uncertainty. *Eng. Struct.* **25**, 1675–1684 (2003)
16. Cheng, J., Jiang, J., Xiao, R., Xiang, H.: Series method for analyzing 3D nonlinear torsional divergence of suspension bridges. *Comput. Struct.* **81**, 299–308 (2003)
17. Boonyapinyo, V., Lauhatanon, Y., Lukkunaprasit, P.: Nonlinear aerostatic stability analysis of suspension bridges. *Eng. Struct.* **28**, 793–803 (2006)
18. Cheng, J., Xiao, R.C.: A simplified method for lateral response analysis of suspension bridges under wind loads. *Commun. Numer. Methods Eng.* **22**, 861–874 (2006)
19. Lacarbonara, W., Arena, A.: Aerostatic torsional divergence of suspension bridges via a fully nonlinear continuum formulation. In: Proc. of 10th National Congress of Wind Engineering IN-VENTO 2008, Cefalù, Italy, 8–11 Jun. (2008)
20. Lacarbonara, W., Arena, A.: 3-dimensional model of suspension bridges via a fully nonlinear continuum formulation. In: Proc. of GIMC 2008, XVII Convegno Italiano di Meccanica Computazionale, Alghero, 10–12 Sept. (2008)
21. Theodorsen, T.: General theory of aerodynamic instability and the mechanism of flutter. NACA REPORT No. 496 (1935)
22. Salvatori, L., Borri, C.: Frequency- and time-domain methods for the numerical modeling of full-bridge aeroelasticity. *Comput. Struct.* **85**, 675–687 (2007)
23. Salvatori, L., Spinelli, P.: Effects of structural nonlinearity and along-span wind coherence on suspension bridge aerodynamics: some numerical simulation results. *J. Wind Eng. Ind. Aerodyn.* **94**, 415–430 (2006)
24. Scanlan, R.H., Tomko, J.J.: Airfoil and bridge deck flutter derivatives. *J. Eng. Mech.* **97**, 1717–1737 (1971)
25. Simiu, E., Scanlan, R.: *H. Wind Effects on Structures—Fundamentals and Applications to Design*, 3rd edn. Wiley-Interscience, New York (1996)
26. Scanlan, R.H.: Reexamination of sectional aerodynamic force functions for bridges. *J. Wind Eng. Ind. Aerodyn.* **89**, 1257–1266 (2001)
27. Agar, T.J.A.: Aerodynamic flutter analysis of suspension bridges by a modal technique. *Eng. Struct.* **11**, 75–82 (1989)
28. Namini, A.H.: Analytical modeling of flutter derivatives as finite elements. *Comput. Struct.* **41**(5), 1055–1064 (1991)
29. Namini, A.H.: Finite element-based flutter analysis of cable-suspended bridge. *J. Struct. Eng.* **118**(6), 1509–1526 (1992)
30. Hua, X.G., Chen, Z.Q.: Full-order and multimode flutter analysis using ANSYS. *Finite Elem. Anal. Des.* **44**, 537–551 (2008)
31. Mishra, S.S., Kumar, K., Krishna, P.: Multimode flutter of long-span cable-stayed bridge based on 18 experimental aeroelastic derivatives. *J. Wind Eng. Ind. Aerodyn.* **96**, 83–102 (2008)
32. Preidikman, S., Mook, D.T.: Numerical simulation of flutter of suspension bridges. *Appl. Mech. Rev.* **50**, 174–179 (1997)
33. Arena, A., Lacarbonara, W.: Static and aeroelastic limit states of Ponte della Musica via a fully nonlinear continuum model. In: Atti del 19mo Congresso dell'Associazione Italiana di Meccanica Teorica e Applicata, Ancona, 14–17 Sept. (2009)
34. Lacarbonara, W., Arena, A.: Flutter of an arch bridge via a fully nonlinear continuum formulation. *J. Aerosp. Eng.* **24**(1), 112–123 (2011)
35. Chen, S.R., Cai, C.S.: Evolution of long-span bridge response to wind-numerical simulation and discussion. *Comput. Struct.* **81**, 2055–2066 (2003)
36. Zhang, X., Sun, B.: Parametric study on the aerodynamic stability of a long-span suspension bridge. *J. Wind Eng. Ind. Aerodyn.* **92**, 431–439 (2004)
37. Zhang, X.: Influence of some factors on the aerodynamic behavior of long-span suspension bridges. *J. Wind Eng. Ind. Aerodyn.* **95**, 149–164 (2007)
38. Pfeil, M.S., Batista, R.C.: Aerodynamic stability analysis of cable-stayed bridges. *J. Struct. Eng.* **121**, 1748–1788 (1995)
39. Ding, Q., Chen, A., Xiang, H.: Coupled flutter analysis of long-span bridges by multimode and full-order approaches. *J. Wind Eng. Ind. Aerodyn.* **90**, 1981–1993 (2002)
40. Cheung, Y.K.: The finite strip method in the analysis of elastic plates with two opposite simply supported ends. *Proc. Inst. Civ. Eng., Lond.* **40**, 1–7 (1968)

41. Lau, D.T., Cheung, M.S., Cheng, S.H.: 3D flutter analysis of bridges by spline finite-strip method. *J. Struct. Eng.* **126**, 1246–1254 (2000)
42. Agar, T.J.A.: The analysis of aerodynamic flutter of suspension bridges. *Comput. Struct.* **30**, 593–600 (1988)
43. Chen, X., Matsumoto, M., Kareem, A.: Time domain flutter and buffeting response analysis of bridges. *J. Eng. Mech.* **126**, 7–16 (2000)
44. Petrini, F., Giuliano, F., Bontempi, F.: Comparison of time domain techniques for the evaluation of the response and the stability in long span suspension bridges. *Comput. Struct.* **85**, 1032–1048 (2007)
45. Singh, L., Jones, N.P., Scanlan, R.H., Lorendeaux, O.: Identification of lateral flutter derivatives of bridge decks. *J. Wind Eng. Ind. Aerodyn.* **60**, 81–89 (1996)
46. Sarkar, P.P., Caracoglia, L., Haan, F.L. Jr., Sato, H., Murakoshid, J.: Comparative and sensitivity study of flutter derivatives of selected bridge deck sections, part 1: analysis of inter-laboratory experimental data. *Eng. Struct.* **31**, 158–169 (2009)
47. Lacarbonara, W.: *Nonlinear Structural Mechanics. Theory, Phenomena and Modeling*. Springer, New York (2012)
48. Antman, S.: *S. Nonlinear Problems of Elasticity*, 2nd edn. Springer, New York (2005)
49. COMSOL Multiphysics 3.5 COMSOL Multiphysics/User's Guide Version 3.5, COMSOL AB (2008)
50. Xiang, H.F.: *Wind-Resistant Design Guidebook for Highway Bridges*. China Communication Press, Beijing (1996) (in Chinese)